

# Open Research Online

---

The Open University's repository of research publications  
and other research outputs

## Anomalously old biotite $^{40}\text{Ar}/^{39}\text{Ar}$ ages in the NW Himalaya

### Journal Item

#### How to cite:

Stübner, Konstanze; Warren, Clare; Ratschbacher, Lothar; Sperner, Blanka; Kleeberg, Reinhard; Pfänder, Jörg and Grujic, Djordje (2017). Anomalously old biotite  $^{40}\text{Ar}/^{39}\text{Ar}$  ages in the NW Himalaya. *Lithosphere*, 9(3) pp. 366–383.

For guidance on citations see [FAQs](#).

© 2017 Geological Society of America



<https://creativecommons.org/licenses/by-nc-nd/4.0/>

Version: Accepted Manuscript

Link(s) to article on publisher's website:  
<http://dx.doi.org/doi:10.1130/L586.1>

---

Copyright and Moral Rights for the articles on this site are retained by the individual authors and/or other copyright owners. For more information on Open Research Online's data [policy](#) on reuse of materials please consult the policies page.

---

[oro.open.ac.uk](http://oro.open.ac.uk)

# Anomalously old biotite $^{40}\text{Ar}/^{39}\text{Ar}$ ages in the NW Himalaya

Konstanze Stübner<sup>1</sup>, Clare Warren<sup>2</sup>, Lothar Ratschbacher<sup>3</sup>, Blanka Sperner<sup>3</sup>, Reinhard Kleeberg<sup>3</sup>, Jörg Pfänder<sup>3</sup>, and Djordje Grujic<sup>4</sup>

<sup>1</sup>*Department of Geosciences, Eberhard Karls University Tübingen, 72074 Tübingen, Germany*

<sup>2</sup>*Department of Earth and Environmental Science, The Open University, Milton Keynes, MK7 6AA, UK*

<sup>3</sup>*Institut für Geologie, Technische Universität Bergakademie Freiberg, 09599 Freiberg, Germany*

<sup>4</sup>*Department of Earth Sciences, Dalhousie University, Halifax, NS B3H 4R2, Canada*

## ABSTRACT

Biotite  $^{40}\text{Ar}/^{39}\text{Ar}$  ages older than corresponding muscovite  $^{40}\text{Ar}/^{39}\text{Ar}$  ages, contrary to the diffusion properties of these minerals, are common in the Himalaya and other metamorphic regions. In these cases, biotite  $^{40}\text{Ar}/^{39}\text{Ar}$  ages are commonly dismissed as ‘too old’ on account of ‘excess Ar’. We present 32 step-heating  $^{40}\text{Ar}/^{39}\text{Ar}$  ages from 17 samples from central Himachal Pradesh Himalaya, India. In almost all cases, the biotite ages are older than predicted from cooling histories. We document host rock lithology and chemical composition, mica microstructures, biotite chemical composition, and chlorite and muscovite components of biotite separates to demonstrate that these factors do not offer an explanation for the anomalously old biotite  $^{40}\text{Ar}/^{39}\text{Ar}$  ages. We discuss possible mechanisms that may account for extraneous Ar (inherited or excess Ar) in these samples. The most likely cause for ‘too-old’ biotite is excess Ar, i.e.  $^{40}\text{Ar}$  that is separated from its parent K. We suggest that this contamination resulted from one or several of the following mechanisms: (1)  $^{40}\text{Ar}$  was released

during Cenozoic prograde metamorphism; (2)  $^{40}\text{Ar}$  transport was restricted due to temporarily dry intergranular medium; (3)  $^{40}\text{Ar}$  was released from melt into a hydrous fluid phase during melt crystallization. Samples from the Main Central Thrust shear zone may be affected by a different mechanism of excess-Ar accumulation, possibly linked to later-stage fluid circulation within the shear zone and chloritization. Different Ar diffusivities and/or solubilities in biotite and muscovite may explain why biotite is more commonly affected by excess Ar than muscovite.

## INTRODUCTION

In most applications, an  $^{40}\text{Ar}/^{39}\text{Ar}$  mineral age is interpreted as the time since cooling through its closure temperature ( $T_c$ ) (Dodson, 1973; McDougall and Harrison, 1999). At temperatures above  $T_c$ , Ar diffuses out of the mineral into an external reservoir; at temperatures below  $T_c$ , Ar is quantitatively retained in the mineral. Dodson (1973) defined the closure temperature as

$$E/(R \times T_c) = \ln(A \times \tau \times D_0/a^2) \quad (1)$$

where  $E$  is the activation energy,  $D_0$  is the diffusion coefficient,  $a$  is the radius of the effective diffusion domain,  $A$  is the grain geometry factor,  $\tau$  is the time constant, and  $R$  is the gas constant. The concept of closure temperature is based on the assumptions that (1) the cooling history is characterized by a linear increase in  $1/T$ ; (2) Ar transport in the mineral is controlled by volume diffusion; (3) Ar escapes into an ‘infinite’ reservoir, and the concentration of Ar at the grain boundary remains zero (‘zero-concentration boundary condition’). Experimental diffusion data suggest that the  $T_c$  of Ar in muscovite and biotite are  $\sim 400\text{-}500^\circ\text{C}$  and  $\sim 300\text{-}400^\circ\text{C}$ , respectively, depending on grain size, mineral chemistry, and cooling rate (Harrison et al., 1985; Grove, 1993; Grove and Harrison, 1996; Harrison et al., 2009).

Mineral  $^{40}\text{Ar}/^{39}\text{Ar}$  ages may deviate from the inferred time of cooling through  $T_c$  for several reasons.  $^{40}\text{Ar}/^{39}\text{Ar}$  ages can be reset by neocrystallization or dynamic recrystallization (e.g., Dunlap 1997; Mulch and Cosca, 2004). Hydrothermal fluids may displace radiogenic  $^{40}\text{Ar}$  through chemical reactions (e.g., Miller et al., 1991). Both mechanisms result in  $^{40}\text{Ar}/^{39}\text{Ar}$  ages that may be younger than the expected cooling ages, depending on the timing of crystallization or fluid flow during cooling. In other cases, calculated  $^{40}\text{Ar}/^{39}\text{Ar}$  ages are ‘too old’; a short metamorphic pulse may be insufficient to completely degas Ar from a mineral (e.g., Viete et al., 2011), or  $^{40}\text{Ar}$  may become trapped, for example, in fluid inclusions (Cumbest et al., 1994) or lattice defects (Camacho et al., 2012). The problem of anomalously old  $^{40}\text{Ar}/^{39}\text{Ar}$  ages is particularly known from biotite (e.g., Roddick et al., 1980; Baxter et al., 2002) and commonly attributed to the presence of excess Ar.

$^{40}\text{Ar}$  from different sources may accumulate in a mineral. Slightly different nomenclature is used throughout the literature; we follow the terminology of Dalrymple and Lanphere (1969) and McDougall and Harrison (1999): Radiogenic Ar is  $^{40}\text{Ar}$  produced within the mineral by radioactive decay of  $^{40}\text{K}$ . Inherited Ar is essentially radiogenic  $^{40}\text{Ar}$  that remained in the mineral during incomplete resetting (e.g., older core with younger rim) or was introduced in the form of older material into the mineral (e.g., older K-bearing particles become incorporated into younger volcanic rocks). Non-radiogenic Ar includes Ar of atmospheric composition (here we use  $^{40}\text{Ar}/^{36}\text{Ar} = 295.5$ ) and excess Ar. Excess Ar is parent-less  $^{40}\text{Ar}$ , i.e.  $^{40}\text{Ar}$  that is separated from its K-bearing source; it is incorporated in rocks and minerals by processes other than in-situ radioactive decay. Trapped Ar was incorporated during mineral formation or at a later event and can encompass atmospheric Ar as well as excess Ar. Inherited and excess Ar—collectively termed extraneous Ar—cause the age of the mineral to appear older than its ‘true’ crystallization or cooling age.



In the Himalaya, many studies have reported biotite  $^{40}\text{Ar}/^{39}\text{Ar}$  ages that were considered ‘too old’ and were therefore excluded from the thermal history interpretations (e.g., Hubbard and Harrison, 1989; Catlos et al., 2001; Stüwe and Foster, 2001; Godin et al., 2006 and references therein; Horton et al., 2014; Adams et al., 2015). Other studies have investigated possible sources of extraneous Ar and tried to link it, for example, to host-rock composition (e.g., Foland, 1979; Boven et al., 2001; Baxter et al., 2002), presence or absence of fluids (e.g., Cumbest et al., 1994; Stüwe and Foster, 2001; Itaya et al., 2009; Halama et al., 2014), or (ultra)-high pressure metamorphism (e.g., Scaillet, 1998; Giorgis et al., 2000; Warren et al., 2011). If extraneous Ar is quantifiable in the system, it may provide additional information about the geologic history of the sample and the physicochemical conditions it experienced (e.g., Kelley and Wartho, 2000).

With the goal of constraining the geological reason(s) behind anomalously old biotite  $^{40}\text{Ar}/^{39}\text{Ar}$  ages in the Himalaya and in metamorphic rocks in general, we present a dataset of biotite and muscovite  $^{40}\text{Ar}/^{39}\text{Ar}$  ages (BtAr, MsAr) from central Himachal Pradesh, NW Himalaya. Petrographic microscope thin section observations, electron microprobe and X-ray diffraction analyses, bulk-rock and mineral composition, and degree of biotite chloritization were used to investigate structural or chemical relationships to the BtAr ages. Isochron analyses of high-resolution step-heating experiments were applied to determine whether this method could usefully detect the presence of excess Ar. The process we outline for determining the likely sources of extraneous Ar are applicable to any metamorphic terrane.

## **GEOLOGIC BACKGROUND**

In central Himachal Pradesh, Cenozoic sediments of the Himalayan foreland were overthrust along the Main Boundary Thrust by the Proterozoic to early Cambrian Lesser

100 Himalayan Sequence (LHS). The Main Central Thrust (MCT), a middle to late Miocene  
101 ductile shear zone, separates the LHS from the Greater Himalayan Sequence (GHS). The  
102 GHS consists of lower greenschist to upper amphibolite facies Haimanta metagreywacke  
103 (Neoproterozoic to Cambrian metapsammite and intercalations of metapelite and calcsilicate)  
104 and Ordovician granite (Thöni, 1977; Steck, 2003; Webb, 2013; Figures 1 and 2). Dominant  
105 foliation, metamorphic isograds and metamorphic zones based on index minerals (Bt + Chl,  
106 Grt, Ky  $\pm$  St  $\pm$  Sil; Wyss, 2000; Steck, 2003; mineral abbreviations after Kretz, 1983) outline  
107 a kilometer-scale, overturned to recumbent, SW-vergent antiform, resulting in an inverse  
108 metamorphic sequence N and NE of the Kullu-Rampur window (overturned limb) and in a  
109 normal metamorphic sequence in the Chandra valley (upper limb, northern study area) and S  
110 and W of the town of Kullu (Figure 2; Thöni, 1977; Epard et al., 1995; Wyss et al., 1999).  
111 The antiform is spectacularly exposed along the western hillslopes of the Beas valley ('Phojal  
112 fold', Figure 2). Although the mechanism and tectonic setting are disputed, the folding is  
113 generally attributed to early Miocene exhumation of mid-crustal rocks by SW-directed  
114 thrusting and folding and accompanying erosion and/or normal faulting (e.g., nappe  
115 emplacement, Epard et al., 1995; extrusion and channel flow, Searle et al., 2007; tectonic  
116 wedging, Webb et al., 2007).

117       Along most of the Himalayan range, the hanging wall of the MCT is cut by the  
118 normal-sense South Tibetan Detachment system (STD), which separates amphibolite-grade  
119 metamorphic rocks of the GHS from the greenschist-facies to unmetamorphosed Tethyan  
120 Himalayan Sequence. In the western Himalaya, the Zaskar Shear Zone and the Sangla  
121 Detachment were identified as strands of the STD, but in central Himachal Pradesh, the  
122 presence and location of shear zones equivalent to the STD are disputed (Thakur, 1998; Wyss  
123 et al., 1999; Webb et al., 2007; Stübner et al., 2014; Figure 1). No strands of the STD system

are depicted in Figures 2A-C, although top-to-the-NE shear does occur, localized along the contacts between intrusive and metamorphic rocks.

The highest-metamorphic grade rocks occur in the core of the Phojal fold (600-700 °C, ~6 kbar; Epard et al., 1995; Leger et al., 2013), below the Deo Tibba Ordovician granite (650-700 °C, ~8 kbar; Wyss, 2000), and in the deeply incised Chandra valley (Ky, St, Hbl, Sil, indicating upper amphibolite facies; Epard et al., 1995; own observations). Here, pegmatite and aplite dikes and veins suggest melting in the latest Eocene and Oligocene (Wyss, 2000; Stübner et al., 2014). We will use the term ‘crystalline core’ to refer to these amphibolite-grade metamorphic rocks (Ky ± Grt zones; Figures 2A-C). North and east of the Kullu-Rampur window, the base of the Haimanta sequence above the MCT has experienced a strong retrograde, greenschist-grade overprint with widespread chloritization of Bt and Grt (Wyss, 2000; Figures 2A-C hatched area). Crustal thickening and prograde metamorphism occurred in the Eocene and Oligocene (~41-26 Ma; Mnz and Grt geochronology; Walker et al., 1999; Thöni et al., 2012; Stübner et al., 2014). The onset of exhumation is recorded by decompression at 26-23 Ma, followed by rapid cooling to ~250 °C at ~30-60 °C/Ma, as constrained by Ms and Bt Rb-Sr and <sup>40</sup>Ar/<sup>39</sup>Ar and zircon fission-track (ZFT) ages (Schlup et al., 2011 and references therein). Most MsAr ages are of 20-22 Ma (total of 20 samples from Walker et al., 1999; Schlup et al., 2011; Stübner et al., 2014). Fewer BtAr dates are reported in the literature, and are in general more variable and include contrasting ages (e.g., 42.6 ± 0.3 Ma and 16.7 ± 0.3 Ma from one locality with a MsAr age of 22.2 ± 0.2 Ma; Schlup et al., 2011). Walker et al. (1999) and Webb et al. (2011) dismissed their BtAr results as geologically meaningless on grounds of excess Ar.

## SAMPLES AND METHODS

Seventeen samples from different lithologies and structural levels of the MCT hanging wall in central Himachal Pradesh were collected for  $^{40}\text{Ar}/^{39}\text{Ar}$  analysis (Table 1). Eleven Bt and 14 Ms separates were analyzed at the Noble Gas Laboratory, Dalhousie University, Halifax, Canada (DGC) (MsAr ages are published in Stübner et al., 2014). Additional three MsAr and four BtAr ages were obtained using finely tuned step-heating experiments at the Argon Lab, Freiberg, Germany (ALF) (Table 2). Analytical details of  $^{40}\text{Ar}/^{39}\text{Ar}$  analysis at both laboratories are given in the supplemental information.

Thin sections were investigated by optical microscopy to characterize the host rocks and micas, with special attention to grain size, texture, and deformation textures such as folding, kinking, undulose extinction, and fracture, indicating intra-crystalline strain (Passchier and Trouw, 2005 and references therein). Backscatter electron (BSE) imaging at high-contrast setting on JEOL JXA 8900 electron microprobes at the Universities of Göttingen and Tübingen was used to characterize compositional variability of Bt in polished thin sections. The same microprobes were used to determine chemical composition (Si, Ti, Fe, Al, Na, K, Mg, Mn, Ca, Ba, Cr, F, Cl) of Bt by wavelength dispersive spectrometry (WDS), using an acceleration voltage of 15 kV, a probe current of 15-20 nA, a beam diameter of 10-20  $\mu\text{m}$ , and counting times of 15 and 60 s on the X-ray signal and total background, respectively. Both core and rim positions were analyzed. For separated grains, grain mounts were used for WDS analysis with a probe current of 7 nA and a beam diameter of 1-2  $\mu\text{m}$ . Biotite chemical formulae were calculated stoichiometrically based on 22 oxygens. In order to assess mineralogical purity of the Bt separates used for  $^{40}\text{Ar}/^{39}\text{Ar}$  thermochronology, X-ray powder-diffraction data were collected by the Rietveld method to quantify the amount of Chl and Ms in Bt separates. Analytical procedures for Rietveld X-ray powder-diffractrometry are described in the supplemental information.

## RESULTS

### Petrography

Petrographic sample descriptions including photomicrographs are provided in the supplemental information (Text and Figure S1). A brief summary is given below and in Table 1. Metasedimentary samples 807D1, 807E1, 811B1, 812D2, and 823G3 (Table 1) are medium to coarse-grained micaschist to metapsammite with a typical assemblage of Qtz + Bt + Ms + Pl  $\pm$  Grt. Biotite is more abundant than Ms, aluminosilicates are not present, and accessory minerals comprise Tur + Ap + Zrn  $\pm$  Aln  $\pm$  Mnz  $\pm$  Ilm  $\pm$  Rt  $\pm$  Czo. Quartz is abundant in all metasedimentary samples. Most samples show minor post-tectonic (across-foliation) growth of Chl or chloritization of Bt and/or Grt. The foliation is pervasive, straight or wavy, and parallel to compositional banding. Biotite lacks evidence of intracrystalline strain (e.g., kinks, undulose extinction). Sample 807E1 has a mm-scale crenulation cleavage with Bt both along the crenulation foliation and within microlithons; the Bt shows no evidence of intracrystalline strain. Sample 814G1 is a fine-grained, banded metapsammite with abundant calcite; large skeletal Ms grains at high angle to the foliation are probably detrital. Sample 827B1 is a fine-grained metapelite with a wavy crenulation cleavage.

Granite and orthogneiss samples are quartz-rich and contain both Bt and Ms, except for 823G2, which lacks Ms (Table 1). Garnet occurs in orthogneiss samples 823G2 and 819A2 and in leucogranite samples 803B3 and 815E1. Similar to the metasedimentary samples, Bt shows no evidence of intracrystalline strain. In augengneiss samples 823G2 and 819A2, Bt forms the main foliation and is intergrown with Grt, suggesting no or little deformation since (re)-crystallization of Bt + Grt. The same textures are observed in the psammitic Haimanta metasedimentary rocks (e.g., 811B1).

## **$^{40}\text{Ar}/^{39}\text{Ar}$ Results**

Table 2 summarizes the  $^{40}\text{Ar}/^{39}\text{Ar}$  results. Age spectra and inverse isochron plots are shown in Figure 3, raw data are reported in Supplemental Tables S1 and S2. Many samples yield high to medium percentages of atmospheric  $^{40}\text{Ar}$  throughout the whole experiment (Figure 3, Table S1). Therefore, the age spectra and the weighted mean ages (WMA) calculated from all heating steps (e.g., Figure 3E, F) or the specified temperature range (e.g., Figure 3A, B) are strongly influenced by the atmospheric correction, such that even small fluctuations in the initial  $^{40}\text{Ar}/^{36}\text{Ar}$  ratio can cause relevant changes in the calculated step ages. For most samples, the interpreted age (rounded values with  $\pm 2\sigma$  error; Table 2) thus relies on the inverse isochron age (IIA), which is unaffected by this type of correction.

A typical experiment at DGC comprised 12-16 heating steps. The age spectra of both Ms and Bt often show complex patterns with only minor plateau sections (e.g., Figure 3B, K, P, Q). Likewise, data in the inverse isochron plots are only partly arranged along single mixing lines between trapped Ar ( $^{36}\text{Ar}/^{40}\text{Ar}$  intercept) and radiogenic Ar ( $^{39}\text{Ar}/^{40}\text{Ar}$  intercept; e.g., Figure 3X, a, b, c). For two experiments, Ms of sample 814G1 and Bt of sample 827B1, the scatter of data was too high to calculate reliable ages, and therefore probable age ranges are suggested in the age interpretation (Figure 3V, g, Table 2). For other samples, IIAs were calculated from all data points, or sometimes excluding the highest- or lowest-temperature heating steps, and typically yielded mean square weighted deviates (MSWD) of  $\leq 5$  (Figure 3, grey error boxes and ellipses and specified temperature range). Initial  $^{40}\text{Ar}/^{36}\text{Ar}$  ratios range from 210 to 420 and are mostly  $\geq 295.5$  (Table 2).

Additional Ms and Bt analyses, using a heating schedule of typically 18-20 steps, were obtained at ALF. All analyses resulted in plateau ages that include 100% of the  $^{39}\text{Ar}$  and with

MSWD <0.6 (Figure 3E, F, N, O, S, T, U; Table 2). These WMAs are identical to the IIAs, which have MSWD <0.3. Initial  $^{40}\text{Ar}/^{36}\text{Ar}$  ratios range from 270 to 340, and all lie within uncertainty of the atmospheric value.

Muscovite ages of most samples range from  $19 \pm 1$  to  $23 \pm 2$  Ma (Table 2, Figures 2 and 3). Muscovite from sample 807E1—analyzed in both labs—yielded indistinguishable ages ( $23 \pm 2$  and  $22 \pm 1$  Ma; Figure 3L, N). Older Ms ages—up to  $64 \pm 5$  Ma—originate from lower-grade metamorphic rocks in the south and north of the study area (Figure 2A). Sample 807D1 yielded a complex age spectrum with step ages increasing from ~33 Ma to 102 Ma with increasing temperature. An inverse isochron, fit to the lowest-temperature degassing steps (800-900 °C), yielded  $27.3 \pm 0.7$  Ma (Figure 3J). Muscovite ages in the Chandra valley increase with elevation from  $20 \pm 1$  Ma (807A1) through  $24 \pm 2$  Ma (807C1) to  $28 \pm 5$  Ma (807D1; Figures 3E, G, J and 2A, elevation profile marked with white box frame).

The BtAr ages are generally older than the MsAr ages from the same locality (compare e.g. Figures 3T and 3U). Most of them range from  $20 \pm 2$  to  $43 \pm 2$  Ma and are thus up to 16 Ma older than the respective MsAr ages (Figures 2A and 4; Table 2). Samples from the MCT zone (823G2, 823G3, and 827B1) yielded pre-Cenozoic BtAr ages ( $84 \pm 6$  Ma;  $106 \pm 5$  Ma; Figure 2B). This inverted age relationship between Bt and Ms was observed irrespective of lithology (c.f. Haimanta metasedimentary rocks vs. orthogneiss), structural position (upper limb vs. core of the Phojal fold), and metamorphic zone (Ky vs. Grt zones; Figures 2A, 2C and 4). The elevation profile in the Chandra valley records a positive age-elevation trend (Figures 2A and 4). A ‘normal’ age relationship between Bt and Ms was revealed for sample 804C1 from the Bt + Chl zone granite (Ms  $64 \pm 5$  Ma, Bt  $31 \pm 2$  Ma) and for sample 807A1 from the Ky zone augengneiss (Ms  $20 \pm 1$  Ma, Bt  $20 \pm 1$  Ma).

## **Biotite Chemistry**

249

250           Electron microprobe analyses of Bt revealed chemical compositions typical for  
251 metamorphic rocks (Guidotti, 1984; Fleet et al., 2003), with 0.21–0.55 Mg/(Mg+Fe), 3.10–  
252 3.47 Al per formula unit (p.f.u.), 0.15–0.33 Ti p.f.u., and low Mn, Ca, Na, Ba, and Cr (Table  
253 3). F is <1.5 wt.%, Cl is close to or below the detection limit of 0.1 wt.%. Total oxides are 93–  
254 97 wt.%. Within each sample, chemical compositions are narrowly defined without detectable  
255 variations between Bt from different textural contexts, i.e., Bt within foliation, in Grt strain  
256 shadows, from inclusions or embayments in Grt, with different grain size, or between cores  
257 and rims. We recognized Chl and marginally chloritized Bt in BSE images in some of the  
258 samples (see Table 1), but with no effects on bulk chemistry and with no correlation to the K-  
259 content.

260

## 261 **Mineralogical Composition of Biotite Separates**

262

263           Powder XRD analyses suggest that the Bt separates used for  $^{40}\text{Ar}/^{39}\text{Ar}$  dating comprise  
264 84–98% Bt (Table 4, Figure 5). Trace amounts (0.6–2.4%) of Chl are present in all analyzed  
265 samples; up to 15% Ms is intergrown with Bt in some samples. Repeated rinsing of the  
266 separates in  $\text{H}_2\text{O}_{\text{dest.}}$  reduced the Ms content (e.g., 812D2: 14% Ms in untreated separate vs.  
267 5% Ms in rinsed separate; Figure 5), but a significant amount of Ms remained after rinsing  
268 (e.g. 807E1: 15% Ms).

269

## 270 **Ti-in-Biotite Thermometry**

271

272           The Ti-in-biotite geothermometer of Henry et al. (2005) yielded Bt equilibration  
273 temperatures of ~360–520 °C; 827B1 did not yield a valid result (not enough Ti, Table 3).



Regional trends in Ti-in-biotite temperatures correspond to the mapped metamorphic zones: The highest temperatures (500-520 °C) were obtained from the center of the crystalline core exposed in the Chandra valley (807E1, 807A1) and in the core of the Phojal fold (815C1); lower temperatures (400-500 °C) were obtained from lower metamorphic-grade rocks (Grt ± Ky zones); the lowest temperatures (<400 °C) were obtained from the structurally highest samples in the upper limb of the Phojal fold (811B1, 807D1; Figure 2B). The elevation profile in the Chandra valley records upsection decreasing temperatures (807A1, 807C1, 807D1; Figure 2C).

## DISCUSSION

### **Do Muscovite and Biotite $^{40}\text{Ar}/^{39}\text{Ar}$ Ages Reflect Cooling through their Closure Temperatures?**

In the metasedimentary rocks (807D1, 807E1, 811B1, 812D2, 815C1, 823G3) foliation-forming Bt and Ms are interpreted to have grown during Oligocene prograde metamorphism (see petrographic descriptions and Figure S1). Only the large skeletal Ms grains in sample 814G1 are likely relict grains. In lower greenschist-grade metapelite 827B1, some mica may be detrital, but most of the coarser grained, foliation-defining Bt and Ms are interpreted as metamorphic. In the orthogneiss and augengneiss samples (806D3, 807A1, 807C1, 810B1, 819A1, 823G2), all mica appears to have recrystallized during the Cenozoic tectonometamorphic cycle. In undeformed and weakly deformed granitic samples, mica grew during magmatic crystallization, i.e., in the Ordovician (Bt and Ms in 804C1) or possibly the Cenozoic (Ms in leucogranites 803B3 and 815E1). With the exception of the detrital grains, there is no indication that one mica phase crystallized later than the other, e.g., as a result of

dynamic recrystallization in shear bands. The inverted age relationship between MsAr and BtAr ages is therefore not a result of post-cooling neocrystallization or recrystallization of Ms.

Metamorphic and magmatic samples from the crystalline core, with 600-700 °C peak metamorphic temperatures (Epard et al., 1995; Wyss, 2000), are expected to yield  $^{40}\text{Ar}/^{39}\text{Ar}$  cooling ages (Warren et al, 2012). With increasing distance from the crystalline core, samples are less likely to have resided at temperatures above Ar closure for a sufficiently long period for complete thermal resetting. Figure 6 provides a compilation of all published as well as our new thermochronologic ages from central Himachal Pradesh. Closure temperatures are  $480 \pm 30$  °C for MsAr and  $350 \pm 30$  °C for BtAr, calculated after equation (1) based on grain radii of 100-400  $\mu\text{m}$  (Table 1), cooling rates of 20-100 °C/Ma, and the diffusion parameters of Harrison et al. (2009) and Grove and Harrison (1996). Monazite geochronologic data indicate prograde metamorphism during ~41-26 Ma and onset of decompression between 26 and 22 Ma (Stübner et al., 2014 and references therein).

Rb-Sr and ZFT thermochronologic data from the crystalline core record early Miocene cooling from 550 to 200 °C at an average rate of ~20 °C/Ma (Figure 6, open red symbols and arrow). The MsAr ages from the crystalline core (19-23 Ma) are consistent with these independent thermochronologic and geochronologic constraints (Figure 6, red solid triangles); they are younger than the Rb-Sr Ms ages and lie on the cooling path defined by the Rb-Sr and ZFT chronometers. In contrast, most of the BtAr ages coincide with the timing of prograde metamorphism and are 10-20 Ma older than what would be expected for cooling ages (Figure 6, red solid circles).

Samples from the northern (Chandra valley, Figure 6, blue symbols) and southern study areas (black symbols) yield more variable Rb-Sr and ZFT ages and are, in general, a few Ma older than those from the crystalline core. The MsAr ages range from ~20 to ~60 Ma (Figure 6, black and blue solid triangles). The MsAr age spectrum of 807D1 (Figure 3G) may

represent a loss profile resulting from partial resetting at  $\leq 28 \pm 5$  Ma (Forster and Lister, 2004; Viete et al., 2011). The MsAr age of 804C1 ( $64 \pm 5$  Ma; Figure 3A) predates the Himalayan prograde metamorphism and may reflect partial resetting of Ms from this Ordovician granite. The BtAr ages from these areas are—with two exceptions—5-10 Ma too old to be interpreted as cooling ages (Figure 2).

Excluding the BtAr ages, the dataset indicates regional rapid exhumation and cooling of the crystalline core since  $\sim 25$  Ma (Figure 6). Age gradients between the younger crystalline core and the slightly older lower-grade rocks may be attributed to diachronous exhumation. The samples from the northern and southern area include rocks from the Grt and Bt + Chl zones. There, residence at peak temperatures may have been insufficient (too short and/or too cold) for complete resetting of the MsAr system, and these analyses may reflect partially reset ages (e.g. 804C1, 803B3, 807D1, 827B1; Figure 6, blue and black solid triangles). Although this interpretation implies that the BtAr ages from these samples are likewise partially reset, it does not offer an explanation for the BtAr ages to be 5-20 Ma older than the corresponding MsAr ages (Figure 2B). Therefore, we interpret the MsAr data as early Miocene cooling ages, with the possible exception of a few samples from the low-grade metamorphic rocks (804C1, 803B3, 807D1, 827B1). BtAr ages are—with the possible exception of samples 814G1 and 807A1—not cooling ages.

#### **Do Biotite $^{40}\text{Ar}/^{39}\text{Ar}$ Ages Correlate with Biotite Equilibration Temperatures?**

The temperature and the portion of the pressure-temperature (P-T) path along which Bt crystallized are important for determining links between the BtAr age and metamorphic evolution. Although the Ti-in-biotite temperatures are consistent with regional metamorphic zoning in the study area, the temperatures are generally 100-200 °C lower than the results

from Bt-Grt thermometry on samples from the same region (600-700 °C; Epard et al., 1995; Wyss, 2000). Several samples do not meet the criteria for which the geothermometer was calibrated, namely graphitic, peraluminous metapelites that contain ilmenite or rutile and have equilibrated at ~4-6 kbar (Henry et al., 2005), suggesting that the temperature estimates may be inaccurate. Biotite in metaluminous samples generally incorporates higher amounts of Ti compared with peraluminous samples (Henry et al., 2005) therefore the calculated temperatures may be upper estimates. Our Ti-in-biotite temperature estimates reveal two characteristics (Figure 7A): (1) The oldest ArBt ages correspond to temperatures  $\leq$  ~400 °C. (2) There is no correlation between ArBt age and Ti-in-biotite temperature above ~400 °C.

#### **Effects of Biotite and Host-rock Chemical Composition on Biotite $^{40}\text{Ar}/^{39}\text{Ar}$ Ages**

The Bt chemical composition of our samples is typical for high-Al metapelitic Bt (Guidotti, 1984; Fleet et al., 2003) and similar to the samples used by Grove and Harrison (1996) for the characterization of Ar diffusion in Bt (Table 3). In particular, Mg/(Fe+Mg) ratios and anion compositions (F/(F+OH)) are comparable to our samples. Increased Ar retentivity—proposed for F-rich and Fe-rich mica (Harrison et al., 1985; Grove and Harrison, 1996)—is thus an unlikely cause for the anomalously old Bt. Similarly, the other elements analyzed (e.g., Ti, Cr, Mn, Ca, Ba, Na) do not show any unusual values. Although the Bt in metasedimentary samples (807D1, 807E1, 812D2, 811B1, 814G1, 815C1, 823G3, 827B1) have slightly higher Mg and lower F content compared to the magmatic samples (807A1, 807C1, 810B1, 823G2; Table 3), the differences are insignificant. Neither the samples that yielded the oldest BtAr ages (823G2, 823G3, 827B1  $\geq$  100 Ma) nor those with BtAr ages consistent with the regionally established cooling paths (807A1, 814G1) reveal any distinct chemical characteristics.

Figure 4 shows BtAr and MsAr ages color-coded by rock type and sorted by their location. There is no obvious correlation between the BtAr age and lithology. However, chemical or mineralogical variations within each of the distinguished rock types are minor: The magmatic rocks have 20-50% quartz, 15-40% plagioclase, 20-40% orthoclase; leucogranite lacks biotite in contrast to granite/orthogneiss, which have biotite and muscovite (see Kreidler, 2014 for chemical characterization of the magmatic rocks in central Himachal Pradesh). The metasedimentary samples were obtained from the psammitic layers within the greywacke sequence and are, therefore, quartz-rich, too. Thus, quartz as a potential local Ar-sink (see discussion below) occurs in all sampled lithologies in similar proportions. Quartz-poor metapelitic layers have not been sampled.

The discrepancy between the BtAr and MsAr ages tends to be larger in the southern part of the study area compared to the north, suggesting that vicinity to the MCT shear zone may be a factor responsible for the anomalous BtAr ages (Figure 4). This conclusion is further supported by samples 823G2 and 823G3 from the MCT zone, which yielded Cretaceous BtAr ages (despite Ti-in-biotite thermometry indicating Bt equilibration at ~430-490 °C during Cenozoic metamorphism) and a MsAr cooling age from sample 823G3 at  $22 \pm 4$  Ma (Table 2, Figure 2A). However, distance to the MCT shear zone does not account for the anomalously old Bt ages from the elevation profile in the Chandra valley, where BtAr ages increase faster with elevation than the MsAr ages do (Figure 4).

### **Effect of Chlorite on Biotite $^{40}\text{Ar}/^{39}\text{Ar}$ Ages**

The effect of chloritization on BtAr data is not well understood but it is known that chloritization might severely disturb age spectra (e.g., Lo and Onstott, 1989). Handpicking of Bt separates is an effective method to remove Chl and partly chloritized Bt in samples that

contain significant amount of Chl. However, our XRF data from four optically Chl-free Bt samples show that ~2% of Chl remained in all separates even after multiple ultrasonic cleaning of the grains (Figure 5, Table 4). Because there is no difference in Chl content between the ‘well-behaved’ (807A1) and ‘too-old’ samples (807E1, 811B1, 812D2; Figure 5), chloritization is unlikely the main cause for the anomalously old Bt ages. On the other hand, samples 823G2, 823G3, and 827B1 from the MCT zone, which yielded pre-Cenozoic BtAr ages, were strongly affected by retrograde metamorphism, accompanied by partial to complete chloritization of Grt. We cannot exclude the possibility that chloritization of Bt contributed to the anomalously old ages of these samples.

#### **Inherited Ar**

The Neoproterozoic to Cambrian Haimanta sedimentary rocks were intruded by Ordovician ( $486 \pm 6$  Ma, Stübner et al., 2014) granite and affected by local contact metamorphism and, possibly, a regional metamorphic overprint (Gehrels et al., 2003). Minerals that have not been reset during Himalayan orogeny may therefore be as old as ~500 Ma, and even small relicts of such old K-bearing minerals and fluid inclusions in Himalayan metamorphic Bt may lead to too-old  $^{40}\text{Ar}/^{39}\text{Ar}$  ages (Figure 8, point 2). The probability that mineral phases and fluid inclusions with an early Paleozoic  $^{40}\text{Ar}$  component survive Cenozoic metamorphism is expected to decrease with the intensity of the metamorphic overprint (e.g., Copeland et al., 1991; Viete et al., 2011; Mottram et al., 2015). We argued earlier that in samples 804C1, 807D1, 814G1, and 827B1 the MsAr system and therefore likely also the BtAr system may be partially reset, i.e. they may include a component of inherited Ar. Older than expected BtAr ages, however, are observed throughout

the study area from the lowest to the highest-grade metamorphic zones (Figures 2B and 6), suggesting that inherited Ar is unlikely to be the main cause of the too-old BtAr ages.

## **Excess Ar**

After ruling out several factors that have previously been suggested to account for anomalously old  $^{40}\text{Ar}/^{39}\text{Ar}$  ages or reverse age relationships between MsAr and BtAr ages, we suggest that excess Ar is the main factor producing too-old BtAr ages in the NW Himalaya. Many previous  $^{40}\text{Ar}/^{39}\text{Ar}$  studies of Himalayan rocks have come to a similar conclusion sometimes leading authors to dismiss or not even present their BtAr ages (e.g., Hubbard and Harrison, 1989; McFarlane, 1993; Vannay and Hodges, 1996; Walker et al., 1999; Godin et al., 2001; Stüwe and Foster, 2001; Stephenson et al., 2001; Horton et al., 2014; Adams et al., 2015), whereas other Himalayan studies report BtAr ages that are unaffected by excess Ar (e.g., Hubbard and Harrison, 1989; Sorkhabi et al., 1993; Guillot et al., 1994; Wang et al., 2006; Leloup et al., 2015).

## ***Inverse Isochron Diagrams Do Not Reveal Excess Ar***

$^{40}\text{Ar}/^{39}\text{Ar}$  step-heating experiments offer, besides age determinations, the opportunity to study the Ar degassing behavior of a specific mineral with increasing heating temperature. In the simplest case, Ar isotopes in the mineral are a mixture between radiogenic and atmospheric Ar, so that the data from the different heating steps plot in the inverse isochron diagram along a straight mixing line with an intercept at the  $^{36}\text{Ar}/^{40}\text{Ar}$ -axis defined by the atmospheric Ar isotope composition (atmospheric  $^{40}\text{Ar}/^{36}\text{Ar} = 295.5$ ). Excess Ar as a third component becomes noticeable if it changes due to its non-atmospheric composition the

$^{36}\text{Ar}/^{40}\text{Ar}$  intercept (commonly stated as its reciprocal, the initial  $^{40}\text{Ar}/^{36}\text{Ar}$  ratio). Usually, excess Ar is enriched in  $^{40}\text{Ar}$ , so that the initial  $^{40}\text{Ar}/^{36}\text{Ar}$  ratio becomes higher. Increased initial  $^{40}\text{Ar}/^{36}\text{Ar}$  values are not uncommon in our experiments, for both Bt and Ms, with values up to  $553 \pm 2$ , but usually scattering between 300 and 350 (Table 2). No correlation between inverse isochron ages and initial  $^{40}\text{Ar}/^{36}\text{Ar}$  ratios is detectable, neither for all data together nor for Ms or Bt alone (Figure 7B). Moreover, the high-resolution BtAr analyses from ALF, for which all heating steps define a plateau age and which show significantly less scatter in the inverse isochron diagrams (Figure 3E, F, N, O, S, T, U), yield trapped  $^{40}\text{Ar}/^{36}\text{Ar}$  values between 270 and 340, all indistinguishable within errors from the atmospheric value (Table 2).

The discussion about the occurrence of excess Ar and its detection from the Ar degassing behavior during step-heating experiments is hampered by the fact that during step-heating, excess  $^{40}\text{Ar}$  may be released together with the radiogenic Ar, the trapped Ar or with both (Kuiper, 2002). If only the trapped Ar component is contaminated with excess  $^{40}\text{Ar}$ , the  $^{36}\text{Ar}/^{40}\text{Ar}$  intercept of the inverse isochron will yield initial  $^{40}\text{Ar}/^{36}\text{Ar} > 295.5$ , but the  $^{39}\text{Ar}/^{40}\text{Ar}$  intercept will reflect only the radiogenic  $^{40}\text{Ar}$ , and the IIA will be unaffected by excess Ar. Conversely, if only the radiogenic component is contaminated by excess  $^{40}\text{Ar}$ , only the age is changed, but not the initial  $^{40}\text{Ar}/^{36}\text{Ar}$  ratio, even though the latter is usually regarded as indication for excess Ar (Kuiper, 2002). This means that the non-existence of increased initial  $^{40}\text{Ar}/^{36}\text{Ar}$  ratios is not a proof for the absence of excess Ar. Therefore, excess Ar may explain the too-old BtAr ages in the Himachal Pradesh despite that fact that initial  $^{40}\text{Ar}/^{36}\text{Ar}$  ratios are not consistently higher than the atmospheric ratio.

#### ***Which Processes May Have Lead to Excess Ar in the Biotite?***



The  $^{40}\text{Ar}/^{39}\text{Ar}$  age dating technique relies on the assumption that Ar concentrations outside of the mineral grain remain close to zero, so that Ar that diffuses out of the mineral grain escapes into an ‘infinite reservoir’ (Figure 8, point 1; e.g., Dodson, 1979). This reservoir may be a local sink, such as a fluid or a host rock mineral with a high Ar solubility, or an external reservoir—ultimately the atmosphere. The ‘total local sink capacity’ is a function of the modes of mineral and fluid phases in the vicinity of the source mineral and their respective Ar partition coefficients; specifically, it has been suggested that the presence or absence of quartz in a rock affects the total local sink capacity and hence controls excess Ar accumulation (Baxter, 2003). In addition, an efficient Ar transport from the Ar-releasing mineral grain into the external reservoir is a critical aspect in  $^{40}\text{Ar}/^{39}\text{Ar}$  thermochronology (e.g., Baxter, 2003). Transport of Ar in a rock volume depends on the presence or absence of fluids in the intergranular space, and it is necessary to distinguish ‘open systems’, in which fluid circulation facilitates rapid transport of Ar over large distances (meters to kilometers), and dry ‘closed systems’, in which transport of Ar is limited to a few centimeters over millions of years (Scaillet, 1996; Kelley, 2002; Baxter, 2003). In dry systems,  $^{40}\text{Ar}$  may accumulate along grain boundaries and partition into minerals resulting in ‘internally’ derived excess Ar; in fluid-rich systems, if the fluid is enriched in  $^{40}\text{Ar}$ , partitioning of  $^{40}\text{Ar}$  into the mineral may result in ‘externally’ derived excess Ar (see Kelley, 2002 and references therein; Baxter, 2007). Here we consider the following (not mutually exclusive) options for excess Ar accumulation:

1. High  $^{40}\text{Ar}$  partial pressure in the intergranular medium (Figure 8, point 3).
2. Dry intergranular medium and/or Cenozoic partial melting disturbing the  $^{40}\text{Ar}$  balance (Figure 8, points 4 and 5).
3. Fluid enriched in  $^{40}\text{Ar}$  resulting in excess Ar incorporation into biotite (Figure 8, point 3).

497 ***High  $^{40}\text{Ar}$  partial pressure in the intergranular medium***

498 Biotite and other K-bearing minerals from the Neoproterozoic/Cambrian Haimanta  
499 metagreywacke and/or Ordovician granite broke down and/or outgassed during Eocene-  
500 Oligocene prograde Barrovian metamorphism, releasing radiogenic  $^{40}\text{Ar}$  ( $^{40}\text{Ar}^*$ ) that had  
501 accumulated over ~500 Ma. A typical Haimanta rock with 3-4 wt%  $\text{K}_2\text{O}$  (Vance and Mahar,  
502 1998; Chambers et al., 2009; Stübner, unpublished data) could result in ~100 ppb  $^{40}\text{Ar}^*$  in the  
503 host rock, assuming  $^{40}\text{Ar}^*$  accumulation over 500 Ma and no Ar loss (see Appendix 1). For  
504 the granite with 6 wt%  $\text{K}_2\text{O}$  (Kreidler, 2014) the  $^{40}\text{Ar}^*$  concentrations would add up to ~200  
505 ppb in a closed system. These  $^{40}\text{Ar}^*$  concentrations are 10-20 times higher than the ~11 ppb  
506  $^{40}\text{Ar}^*$  that would have accumulated in a Bt with 10 wt.%  $\text{K}_2\text{O}$  over ~20 Ma, and could  
507 significantly disturb the  $^{40}\text{Ar}^*$  budget of Bt and other mineral phases. High Ar partial pressure  
508 in the intergranular space in combination with the lower Ar solubility in Ms than Bt may  
509 result in partitioning of  $^{40}\text{Ar}$  into Bt in preference to Ms (Figure 8, point 3) (see Kelley, 2002  
510 for a recent summary of Ar solubility). This mechanism predicts that metasedimentary and  
511 magmatic rocks are both affected by excess Ar, depending on their respective mineralogical  
512 composition (e.g., quartz content) and K concentration (Baxter, 2003). This may explain why  
513 both magmatic and metasedimentary samples are affected by excess Ar (Figure 4), but it does  
514 not provide a straightforward explanation why BtAr ages from the MCT zone are significantly  
515 more affected by excess Ar than samples from the MCT hanging wall.

516  
517 ***Dry intergranular medium and Cenozoic partial melting disturb the  $^{40}\text{Ar}$  balance***

518 Solubility of Ar in hydrous fluids is 4-5 orders of magnitude higher than in most  
519 minerals (see compilation in Kelley, 2002) providing an effective local sink for Ar as well as  
520 serving as pathway to a more external sink (Baxter, 2003; Baxter et al., 2007; Figure 8, point  
521 1). For dry systems, it has been shown both experimentally (Baxter et al., 2007) and in field

studies (Foland, 1979; Scailliet, 1996) that restricted mobility of Ar ensues accumulation of <sup>40</sup>Ar in the intergranular medium and can result in excess Ar in minerals.

In the Himachal Himalaya, there is ample evidence for fluid circulation throughout the Cenozoic. Examples are: (1) Ubiquitous quartz segregation veins are associated with early to late Himalayan deformation and metamorphism (e.g., Epard et al., 1995; Wyss et al., 1999). (2) Tourmaline is one of the main accessory phases in the Haimanta metasedimentary rocks. (3) Ky + Qtz segregation veins are common and indicate the presence of aqueous fluids during amphibolite-facies metamorphism. (4) Pegmatite dikes intruded along the axial surfaces of folds are related to the late stages of thrusting along the MCT and formation of the Phojal fold in the late Oligocene-early Miocene (Epard et al., 1995; own observations). We therefore consider it unlikely that dry conditions existed throughout the entire Cenozoic metamorphic cycle.

It is, however, conceivable that partial melting and melt extraction consumed hydrous fluids, resulting in locally dry pore spaces (Figure 8, point 4). The NW Himalaya was affected by a protracted history of crustal melting between ~36 and 18 Ma (e.g., Dèzes et al., 1999; Robyr et al., 2006; Langille et al., 2012; Lederer et al., 2013; Stübner et al., 2014), similar to other locations in the Himalaya (e.g., Rubatto et al., 2013; Zeiger et al., 2015). Removal of hydrous fluids by late Eocene-Oligocene migmatization could have significantly reduced the total local sink capacity (Baxter, 2003), resulting in accumulation of excess Ar. However, most if not all of our Bt samples are from rocks that did not undergo partial melting; for dry conditions to have affected the BtAr ages, migmatization and melt extraction must have affected the fluid budget on a several-kilometer scale. In this case, it is theoretically possible that the excess-Ar Bt ages provide a maximum age estimate of migmatization.

Silicate melts have Ar solubilities intermediate between those of hydrous fluids and most minerals (e.g., Kelley, 2002 and references therein). During migmatization, melts are

likely to serve as an additional sink for intergranular  $^{40}\text{Ar}$ . During melt crystallization,  $^{40}\text{Ar}$  may be released back into the intergranular medium, increasing its  $^{40}\text{Ar}$  concentration. Consequently, excess Ar may diffuse from the intergranular medium into the mineral phases for as long as the rocks reside at temperatures above  $T_c$  (Figure 8, point 5). Some Himalayan Miocene leucogranite yields geologically reasonable BtAr ages, reflecting the timing of emplacement and cooling (e.g., Copeland et al., 1990; Hodges et al., 1998; Wang et al., 2006), whereas in other locations, the BtAr ages are apparently affected by excess Ar (Horton et al., 2014). Therefore, migmatization does not offer a straightforward explanation for excess BtAr ages in the study area or in the Himalayan orogen in general.

Migmatization and melt emplacement may be related to accumulation of excess Ar in minerals through two effects: (1) It affects the availability of hydrous fluids in the pore space, and (2) the high solubility of Ar in melt affects the distribution of  $^{40}\text{Ar}$  in melt, hydrous fluid and mineral phases. A better understanding of these mechanisms requires determination of partition coefficients of Ar between silicate melt, hydrous fluids, and mineral phases, in particular for Ms and Bt.

### ***Fluid circulation along the MCT***

In the NW Himalaya, the MCT was active between ~26-23 Ma and ~17-15 Ma (e.g., Stephenson et al., 2001; Vannay et al., 2004). This thrust activity was associated with intense fluid circulation, causing retrograde greenschist-facies metamorphism with chloritization of Bt and Grt and formation of cm- to dm-sized quartz veins within the ~3 km wide shear zone (e.g., Wyss, 2000). Circulation of fluids has been documented along the entire MCT shear zone, for example, in Nepal (Copeland et al., 1991; Evans et al., 2008; Derry et al., 2009) and Bhutan (Stüwe and Foster, 2001; Mottram et al., 2015), where it was proposed to account for excess Ar in Bt and a reverse relationship between MsAr and BtAr ages. In central Himachal

Pradesh, two MsAr ages from the MCT shear zone and its immediate hanging wall are geologically reasonable: 823G3 ( $22 \pm 4$  Ma) is indistinguishable from other MsAr cooling ages from the hanging wall crystalline rocks; 827B1 ( $32 \pm 9$  Ma) is consistent with other thermochronometric ages from the same locality (Figure 2A). In contrast, Bt from these samples yielded pre-Cenozoic  $^{40}\text{Ar}/^{39}\text{Ar}$  ages, significantly older than any other BtAr ages from the study area and predating Cenozoic prograde metamorphism.

Studies on the composition of modern hydrothermal fluids along the MCT suggest a large component of meteoric water (e.g., Derry et al., 2009), but the Ar isotopic composition of these fluids is unknown. High partial pressures of Ar of any isotopic composition can slow or inhibit diffusive loss of radiogenic  $^{40}\text{Ar}$  from the mineral, thus leading to accumulation of internally derived excess Ar (e.g., Baxter, 2003). In the end-member scenario of high Ar partial pressure in the intergranular medium blocking diffusional escape of radiogenic  $^{40}\text{Ar}$ , the excess Ar Bt age could theoretically record the time when the intergranular medium became saturated in Ar. Therefore, the pre-Cenozoic BtAr ages from three samples from the MCT zone (827B1, 823G2, 823G3) cannot be attributed to an influx of atmospheric Ar in the late Oligocene-Miocene alone. If anomalous BtAr ages from the MCT zone result from fluid circulation within the MCT shear zone, as suggested by the spatial correlation in the study area and by  $^{40}\text{Ar}/^{39}\text{Ar}$  thermochronology studies in other localities in the Himalaya (Hubbard and Harrison, 1989; Stüwe and Foster, 2001), these hydrous fluids must have been enriched in  $^{40}\text{Ar}$  (Figure 8, point 3). The source of this  $^{40}\text{Ar}$  may, for example, be prograde metamorphic Ar release (see above). Possible mechanisms leading to excess Ar in Bt include partitioning of  $^{40}\text{Ar}$  from the fluid phase into the mineral or trapping in fluid inclusions. Because the Bt samples from the MCT zone are an order of magnitude more strongly affected by excess Ar than the hanging-wall samples (Cretaceous vs. Cenozoic BtAr ages), and excess Ar in the hanging wall samples does not vary systematically with distance to the MCT (Figure 4), we

suggest that various, although possibly related mechanisms account for excess Ar in the MCT zone and in the hanging wall, respectively.

## CONCLUSIONS

Most of the BtAr ages yielded from granitic and metapelitic samples from Himachal Pradesh are older than MsAr ages from the same samples and 5-20 Ma older than the expected timing of cooling through BtAr closure temperature derived from independent geochronologic evidence. Apart from BtAr ages from the MCT zone, which are pre-Cenozoic, BtAr ages tend to cluster at 20-40 Ma. The 'too-old' BtAr ages do not correlate with lithology or structural position. The Bt separates contain only ~2 % Chl, suggesting that chloritization is not the main cause for these anomalously old BtAr ages.

We suggest that the likely cause for the 'too-old' BtAr ages in the Himachal Pradesh is excess Ar in Bt but not, or to a lesser extent, in Ms. Possible sources of excess Ar are:

- (1)  $^{40}\text{Ar}$  released from older K-bearing minerals during Cenozoic prograde metamorphism and mineral breakdown, which partitioned into Bt and/or inhibited diffusive loss of radiogenic  $^{40}\text{Ar}$  at high temperature;
- (2)  $^{40}\text{Ar}$  that accumulated in Bt at temperatures above  $T_c$  because a temporarily dry intergranular medium, possibly resulting from late Eocene-Oligocene migmatization and melt extraction, restricted  $^{40}\text{Ar}$  transport towards an external sink;
- (3)  $^{40}\text{Ar}$  released from melt into a hydrous fluid phase during Oligocene melt crystallization resulting in high  $^{40}\text{Ar}$  concentrations in the rock and partitioning of  $^{40}\text{Ar}$  into Bt.

Samples from the MCT shear zone yield significantly older BtAr ages than samples from the hanging wall rocks and may be affected by a different mechanism of excess-Ar

621 accumulation, possibly linked to fluid circulation within the MCT zone and strong  
622 chloritization.

623         The proposed mechanisms of excess-Ar accumulation in Bt depend on the solubility  
624 of Ar in minerals, hydrous fluids and melts, and further experiments that determine partition  
625 coefficients between these phases will provide further insight into the problem of excess Ar;  
626 in particular, although it is accepted that solubility of Ar in minerals is an order of magnitude  
627 lower than in hydrous fluids, the partition coefficients between different mineral phases is  
628 poorly known (see compilation in Kelley, 2002). Excess Ar is more commonly detected in Bt  
629 than in Ms, possibly due to higher solubility of Ar in Bt compared to Ms. This makes Bt more  
630 susceptible to excess-Ar accumulation if the zero-Ar boundary condition is violated in an  
631 open or closed system. The higher susceptibility of Bt to excess Ar compared to Ms could  
632 also be due to its diffusion characteristics, with its higher Ar diffusivity responsible for  
633 incorporation of more excess Ar in cases where a surplus is available in the intergranular  
634 medium. This surplus can be provided by Ar-enriched fluids or might be an effect of Ar  
635 accumulation under dry conditions (closed system), but it can also be caused by an increasing  
636 partition coefficient between mineral and fluid during post-metamorphic cooling (Kelley,  
637 2002). Decreasing solubility of Ar in fluids at decreasing temperatures triggers its diffusion  
638 into the solid phase, preferentially into minerals with high Ar diffusivity and thus more  
639 readily into Bt compared to Ms. These considerations suggest that in most sample sets, in  
640 which Bt is affected by excess Ar it is most likely that Ms, too, contains excess Ar, although  
641 its concentrations are probably smaller and may not affect  $^{40}\text{Ar}/^{39}\text{Ar}$  ages.

## 643 **APPENDIX 1. Calculation of $^{40}\text{Ar}$ accumulation**

644         Assuming 3.5 wt%  $\text{K}_2\text{O}$  in Haimanta sediments and using molar masses  $\text{K}_2 = 2 \times 39.1$   
645 g/mol and  $\text{K}_2\text{O} = 94.2$  g/mol, the amount of K in Haimanta sediments is  $3.5 \times (2 \times 39.1 /$

94.2) = 2.91 wt% K<sub>2</sub>. Using the molar fraction of <sup>40</sup>K/K = 0.000117 the amount of <sup>40</sup>K in the sediment is 0.000117 × (2.91/100) × 1E+6 = 3.4 ppm <sup>40</sup>K or 3.4 mg <sup>40</sup>K per 1 kg rock. The decay of <sup>40</sup>K to <sup>40</sup>Ar\* is calculated after McDougall and Harrison (1999, Eq. 2.11). For t = 500 Ma the amount of <sup>40</sup>Ar\* is 0.114 ppm (0.114 mg <sup>40</sup>Ar per 1 kg rock). For Ordovician granite with typically 6 wt% K<sub>2</sub>O (Kreidler, 2014), the same calculation yields 0.684 ppm <sup>40</sup>Ar accumulated over 500 Ma.

## ACKNOWLEDGEMENTS

This study was funded by DFG grant STU525/1. Fieldwork and analytical work by DG was supported by the Natural Sciences and Engineering Research Council of Canada (Discovery grant RGPIN 04297). ALF operation was supported by DFG grant Ra 442/37. KS acknowledges financial support by the Excellence Initiative of Univ. Tübingen and the Athene Program. Tashi Tsering assisted with field work. Andreas Kronz (Univ. Göttingen) and Thomas Wenzel (Univ. Tübingen) helped with electron microprobe analyses; Heiner Taubald (Univ. Tübingen) conducted whole rock XRF analyses. We are thankful for the constructive comments of Y. Kuiper, P.H. Leloup, E. Baxter and an anonymous reviewer, which improved an earlier version of this manuscript, and we thank Damian Nance for editorial handling.

## REFERENCES CITED

- Adams, B.A., Hodges, K.V., Whipple, K.X., Ehlers, T., van Soest, M.C., and Wartho, J.-A., 2015, Constraints on the tectonic and landscape evolution of the Bhutan Himalaya from thermochronometry: *Tectonics*, v. 34, no. 6, p. 1329–1347, doi: 10.1002/2015TC003853.
- Baxter, E.F., DePaolo, D.J., and Renne, P.R., 2002, Spatially correlated anomalous <sup>40</sup>Ar/<sup>39</sup>Ar ‘Age’ variations about a lithologic contact near Simplon Pass, Switzerland: A



671 mechanistic explanation for excess Ar: *Geochimica Cosmochimica Acta*, v. 66, p. 1067–  
672 1083.

673 Baxter, E.F., 2003, Quantification of the factors controlling the presence of excess  $^{40}\text{Ar}$  or  
674  $^4\text{He}$ : *Earth and Planetary Science Letters*, v. 216, p. 619–634.

675 Baxter, E.F., Asimow, P.D., and Farley, K.A., 2007, Grain boundary partitioning of Ar and  
676 He: *Geochimica et Cosmochimica Acta*, v. 71, no. 2, p. 434–451.

677 Boven, A., Pasteels, P., Kelley, S.P., Punzalan, L., Bingen, B., and Demaiffe, D., 2001,  
678  $^{40}\text{Ar}/^{39}\text{Ar}$  study of plagioclases from the Rogaland anorthosite complex (SW Norway); an  
679 attempt to understand argon ages in plutonic plagioclase: *Chemical Geology*, v. 176, no.  
680 1, p. 105–135.

681 Camacho, A., Lee, J.K., Gerald, J.F., Zhao, J., Abdu, Y.A., Jenkins, D.M., Hawthorne, F.C.,  
682 Kyser, T.K., Creaser, R.A., Armstrong, R., and Heaman, L.W., 2012, Planar defects as  
683 Ar traps in trioctahedral micas: A mechanism for increased Ar retentivity in phlogopite:  
684 *Earth and Planetary Science Letters*, v. 341, p. 255–267.

685 Catlos, E.J., Harrison, T.M., Kohn, M.J., Grove, M., Ryerson, F.J., Manning, C.E., and  
686 Upreti, B.N., 2001, Geochronologic and thermobarometric constraints on the evolution of  
687 the Main Central Thrust, central Nepal Himalaya: *Journal of Geophysical Research*:  
688 *Solid Earth*, v. 106, no. B8, p. 16177–16204.

689 Chambers, J., Caddick, M., Argles, T., Horstwood, M., Sherlock, S., Harris, N., Parrish, R.,  
690 and Ahmad, T., 2009, Empirical constraints on extrusion mechanisms from the upper  
691 margin of an exhumed high-grade orogenic core, Sutlej valley, NW India:  
692 *Tectonophysics*, v. 477, p. 77–92.

693 Copeland, P., Harrison, M.T., and Le Fort, P., 1990, Age and cooling history of the Manaslu  
694 granite: implications for Himalayan tectonics: *Journal of Volcanology and Geothermal*  
695 *Research*, v. 44, no. 1, p. 33–50.

696 Copeland, P., Harrison, T.M., Hodges, K.V., Maruéjol, P., Le Fort, P., and Pêcher, A., 1991,  
 697 An early Pliocene thermal disturbance of the Main Central Thrust, central Nepal:  
 698 Implications for Himalayan tectonics: *Journal of Geophysical Research: Solid Earth*, v.  
 699 96, no. B5, p. 8475–8500.

700 Cumest R.J., Johnson E.L., and Onstott, T.C., 1994, Argon composition of metamorphic  
 701 fluids: Implications for  $^{40}\text{Ar}/^{39}\text{Ar}$  geochronology: *Geological Society of America*  
 702 *Bulletin*, v. 106, p. 942–951.

703 Dalrymple, G.B., and Lanphere, M.A., 1969, Potassium–Argon Dating, Principle Techniques  
 704 and Applications to Geochronology: Freeman, San Francisco, 258 p.

705 Derry, L.A., Evans, M.J., Darling, R., and France-Lanord, C., 2009, Hydrothermal heat flow  
 706 near the Main Central thrust, central Nepal Himalaya: *Earth and Planetary Science*  
 707 *Letters*, v. 286, no. 1, p. 101–109.

708 Dèzes, P.J., Vannay, J.-C., Steck, A., Bussy, F., and Cosca, M., 1999, Synorogenic extension:  
 709 quantitative constraints on the age and displacement of the Zaskar shear zone (northwest  
 710 Himalaya): *Geological Society of America Bulletin*, v. 111, p. 364–374, doi:  
 711 10.1130/0016-7606(1999)111b0364:SEQCOTN2.3.CO;2.

712 Dodson, M.H., 1973, Closure temperature in cooling geochronological and petrological  
 713 systems: *Contributions to Mineralogy and Petrology*, v. 40, p. 259–274.

714 Dunlap, W.J., 1997, Neocrystallization or cooling?  $^{40}\text{Ar}/^{39}\text{Ar}$  ages of white micas from low-  
 715 grade mylonites: *Chemical Geology*, v. 143, no. 3, p. 181–203.

716 Epard, J.-L., Steck, A., Vannay, J.-C., and Hunziker, J., 1995, Tertiary Himalayan structures  
 717 and metamorphism in the Kulu Valley (Mandi-Khoksar transect of the Western  
 718 Himalaya)—Shikar-Beh-Nappe and Crystalline Nappe: *Schweizerische Mineralogische*  
 719 *und Petrographische Mitteilungen*, v. 75, p. 59–84.

720 Evans, M.J., Derry, L.A., and France-Lanord, C., 2008, Degassing of metamorphic carbon  
 721 dioxide from the Nepal Himalaya: *Geochemistry Geophysics Geosystems*, v. 9, no. 4,  
 722 doi: 10.1029/2007GC001796.

723 Fleet, M.E., Deer, W.A., Howie, R.A., and Zussman, J., 2003, *Rock-forming minerals. Sheet*  
 724 *silicates. Micas*: Geological Society London, 765 p.

725 Foland, K.A., 1979, Limited mobility of argon in a metamorphic terrain: *Geochimica et*  
 726 *Cosmochimica Acta*, v. 43, p. 793–801.

727 Forster, M.A., and Lister, G.S., 2004, The interpretation of  $^{40}\text{Ar}/^{39}\text{Ar}$  apparent age spectra  
 728 produced by mixing: application of the method of asymptotes and limits: *Journal of*  
 729 *Structural Geology*, v. 26, no. 2, p. 287–305.

730 Gehrels, G.E., DeCelles, P.G., Martin, A., Ojha, T.P., Pinhassi, G., and Upreti, B.N., 2003,  
 731 Initiation of the Himalayan orogen as an early Paleozoic thin-skinned thrust belt: *GSA*  
 732 *Today*, v. 13, no. 9, p. 4–9.

733 Giorgis, D., Cosca, M.A., and Li, S., 2000, Distribution and significance of extraneous argon  
 734 in UHP eclogite (Sulu terrane, China): insights from in-situ  $^{40}\text{Ar}/^{39}\text{Ar}$  UV-laser ablation  
 735 analysis: *Earth and Planetary Science Letters*, v. 181, p. 605–615.

736 Godin, L., Parrish, R.R., Brown, R.L. and Hodges, K.V., 2001, Crustal thickening leading to  
 737 exhumation of the Himalayan metamorphic core of central Nepal: Insight from U-Pb  
 738 geochronology and  $^{40}\text{Ar}/^{39}\text{Ar}$  thermochronology: *Tectonics*, v. 20, no. 5, p.729–747.

739 Godin, L., Gleeson, T.P., Searle, M.P., Ullrich, T.D., and Parrish, R.R., 2006, Locking of  
 740 southward extrusion in favour of rapid crustal-scale buckling of the Greater Himalayan  
 741 sequence, Nar valley, central Nepal. In: Law, R.D., Searle, M.P., and Godin, L. (Eds),  
 742 *Channel Flow, Ductile Extrusion and Exhumation in Continental Collision Zones*:  
 743 Geological Society London, Special Publications, v. 268, no. 1, p. 269-292.

744 Grove, M., and Harrison, T.M., 1996,  $^{40}\text{Ar}^*$  diffusion in Fe-rich biotite: American  
745 Mineralogist, v. 81, p. 940–951.

746 Grove, M., 1993, Thermal histories of Southern California basement terranes [Ph.D. thesis]:  
747 University of California, Los Angeles, 419 p.

748 Guidotti, C.V., 1984, Micas in metamorphic rocks: Reviews in Mineralogy and  
749 Geochemistry, v. 13, no. 1, p. 357–467.

750 Guillot, S., Hodges, K., Le Fort, P., and Pêcher, A., 1994, New constraints on the age of the  
751 Manaslu leucogranite: Evidence for episodic tectonic denudation in the central  
752 Himalayas: Geology, v. 22, no. 6, p. 559–562.

753 Halama, R., Konrad-Schmolke, M., Sudo, M., Marschall, H.R., and Wiedenbeck, M., 2014,  
754 Effects of fluid–rock interaction on  $^{40}\text{Ar}/^{39}\text{Ar}$  geochronology in high-pressure rocks  
755 (Sesia-Lanzo Zone, Western Alps): Geochimica et Cosmochimica Acta, v. 126, p. 475–  
756 494.

757 Harrison, T.M., Duncan, I., and McDougall, I., 1985, Diffusion of  $^{40}\text{Ar}$  in biotite:  
758 Temperature, pressure and compositional effects: Geochimica et Cosmochimica Acta, v.  
759 49, no. 11, p. 2461–2468.

760 Harrison, T.M., Célérier, J., Aikman, A.B., Hermann, J., and Heizler, M.T., 2009, Diffusion  
761 of  $^{40}\text{Ar}$  in muscovite: Geochimica et Cosmochimica Acta, v. 73, no. 4, p. 1039–1051.

762 Henry, D.J., Guidotti, C.V., and Thomson, J.A., 2005, The Ti-saturation surface for low-to-  
763 medium pressure metapelitic biotites: Implications for geothermometry and Ti-  
764 substitution mechanisms: American Mineralogist, v. 90, no. 2-3, p. 316–328.

765 Hodges, K., Bowring, S., Davidek, K., Hawkins, D., and Krol, M., 1998, Evidence for rapid  
766 displacement on Himalayan normal faults and the importance of tectonic denudation in  
767 the evolution of mountain ranges: Geology, v. 26, no. 6, p. 483–486.

768 Horton, F., Lee, J., Hacker, B., Bowman-Kamaha'o, M., and Cosca, M., 2015, Himalayan  
 769 gneiss dome formation in the middle crust and exhumation by normal faulting: New  
 770 geochronology of Gianbul dome, northwestern India: Geological Society of America  
 771 Bulletin, v. 127, no. 1-2, p. 162–180, doi: 10.1130/B31005.1.

772 Hubbard, M.S., and Harrison, T.M., 1989,  $^{40}\text{Ar}/^{39}\text{Ar}$  age constraints on deformation and  
 773 metamorphism in the Maine Central Thrust zone and Tibetan Slab, eastern Nepal  
 774 Himalaya: Tectonics, v. 8, no. 4, p. 865–880.

775 Itaya, T., Hyodo, H., Tsujimori, T., Wallis, S., Aoya, M., Kawakami, T., and Gouzu, C., 2009,  
 776 Regional-scale excess Ar wave in a Barrovian type metamorphic belt, eastern Tibetan  
 777 Plateau: Island Arc, v. 18, p. 293–305.

778 Jenkin, G.R., 1997, Do cooling paths derived from mica Rb-Sr data reflect true cooling paths?  
 779 Geology, v. 25, no. 10, p. 907–910.

780 Kelley, S.P., 2002, Excess argon in K-Ar and Ar-Ar geochronology: Chemical Geology, v.  
 781 188, no. 1-2, p. 1–22.

782 Kelley, S.P., and Wartho, J.-A., 2000, Rapid kimberlite ascent and the significance of Ar-Ar  
 783 ages in xenolith phlogopites: Science, v. 289, p. 609–611.

784 Kreidler, M., 2014, Geochemische Untersuchung von ausgewählten proterozoischen und  
 785 paläozoischen Granitoiden aus dem Himachal Pradesh (Nordwest Indien) in Anbetracht  
 786 einer frühpaläozoischen Orogenese, sowie ein Vergleich mit Literaturwerten [BSc  
 787 thesis]: University Tübingen, Germany, 44 p. (in German).

788 Kretz, R., 1983, Symbols for rock-forming minerals: American Mineralogist, v. 68, no. 1-2, p.  
 789 277–279.

790 Kuiper, Y.D., 2002, The interpretation of inverse isochron diagrams in  $^{40}\text{Ar}/^{39}\text{Ar}$   
 791 geochronology: Earth and Planetary Science Letters, v. 203, no. 1, p. 499–506.

792 Langille, J.M., Jessup, M.J., Cottle, J.M., Lederer, G., and Ahmad, T., 2012, Timing of  
 793 metamorphism, melting and exhumation of the Leo Pargil dome, northwest India: Journal  
 794 of Metamorphic Geology, v. 30, p. 769–791, doi: 10.1111/j.1525-1314.2012.00998.x.  
 795 Lederer, G.W., Cottle, J.M., Jessup, M.J., Langille, J.M., and Ahmad, T., 2013, Timescales of  
 796 partial melting in the Himalayan middle crust: insight from the Leo Pargil dome,  
 797 northwest India: Contributions to Mineralogy and Petrology, v. 166, no. 5, p. 1415–1441.  
 798 Leger, R.M., Webb, A.A.G., Henry, D.J., Craig, J.A., and Dubey, P., 2013, Metamorphic field  
 799 gradients across the Himachal Himalaya, northwest India: Implications for the  
 800 emplacement of the Himalayan crystalline core: Tectonics, v. 32, no. 3, p. 540–557.  
 801 Leloup, P.H., Liu, X., Mahéo, G., Paquette, J.L., Arnaud, N., Aubray, A., and Liu, X., 2015,  
 802 New constraints on the timing of partial melting and deformation along the Nyalam  
 803 section (central Himalaya): implications for extrusion models: Geological Society,  
 804 London, Special Publications, v. 412, no. 1, p. 131–175.  
 805 Lo, C.H., and Onstott, T.C., 1989,  $^{39}\text{Ar}$  recoil artifacts in chloritized biotite: Geochimica et  
 806 Cosmochimica Acta, v. 53, no. 10, p. 2697–2711.  
 807 Ludwig, K.R., 2008, Isoplot 4.15. A geochronological toolkit for Microsoft Excel: Berkeley  
 808 Geochronology Center Special Publication, v. 4, 76 p.  
 809 MacFarlane, A.M., 1993, Chronology of tectonic events in the crystalline core of the  
 810 Himalaya, Langtang National Park, central Nepal: Tectonics, v. 12, no. 4, p. 1004–1025.  
 811 McDougall, I., and Harrison, T.M., 1999, Geochronology and Thermochronology by the  
 812  $^{40}\text{Ar}/^{39}\text{Ar}$  Method: Oxford University Press, New York, 269 p.  
 813 Mehta, P.K., 1977, Rb-Sr geochronology of the Kulu-Mandi belt: its implications for the  
 814 Himalayan tectogenesis: Geologische Rundschau, v. 66, no. 1, p. 156–175.

815 Miller, W.M., Fallick, A.E., Leake, B.E., Macintyre, R.M., and Jenkin, G.R.T., 1991, Fluid  
816 disturbed hornblende K-Ar ages from the Dalradian rocks of Connemara, Western  
817 Ireland: *Journal of the Geological Society*, v. 148, no. 6, p. 985–992.

818 Mottram, C.M., Warren, C.J., Halton, A.M., Kelley, S.P., and Harris, N.B., 2015, Argon  
819 behaviour in an inverted Barrovian sequence, Sikkim Himalaya: The consequences of  
820 temperature and timescale on  $^{40}\text{Ar}/^{39}\text{Ar}$  mica geochronology: *Lithos*, v. 238, p. 37–51.

821 Mulch, A., and Cosca, M.A., 2004, Recrystallization or cooling ages: in situ UV-laser  
822  $^{40}\text{Ar}/^{39}\text{Ar}$  geochronology of muscovite in mylonitic rocks: *Journal of the Geological*  
823 *Society*, v. 161, no. 4, p. 573–582.

824 Passchier, C.W., and Trouw, R.A.J., 2005, *Microtectonics*: Springer, Berlin, 366 p.

825 Robyr, M., Hacker, B.R., Mattison, J.M., 2006, Doming in compressional orogenic settings:  
826 new geochronological constraints from the NW Himalaya: *Tectonics*, v. 25, no. 2, doi:  
827 10.1029/2004TC001774.

828 Roddick, J.C., Cliff, R.A., Rex, D.C., 1980, The evolution of excess argon in alpine biotites—  
829 A  $^{40}\text{Ar}$ - $^{39}\text{Ar}$  analysis: *Earth and Planetary Science Letters*, v. 48, no. 1, p. 185–208.

830 Rubatto, D., Chakraborty, S., and Dasgupta, S., 2013, Timescales of crustal melting in the  
831 Higher Himalayan Crystallines (Sikkim, Eastern Himalaya) inferred from trace element-  
832 constrained monazite and zircon chronology: *Contributions to Mineralogy and Petrology*,  
833 v. 165, no. 2, p. 349–372.

834 Scaillet, S., 1996, Excess  $^{40}\text{Ar}$  transport scale and mechanism in high-pressure phengites: A  
835 case study from an eclogitized metabasite of the Dora-Maira nappe, western Alps:  
836 *Geochimica et Cosmochimica Acta*, v. 60, no. 6, p. 1075–1090.

837 Scaillet, S., 1998, K-Ar ( $^{40}\text{Ar}/^{39}\text{Ar}$ ) geochronology of ultrahigh pressure rocks. In: Hacker,  
838 B.R., Liou, J.G. (Eds), *When continents collide: Geodynamics and geochemistry of*  
839 *ultrahigh-pressure rocks*, Springer Netherlands, p. 161–201.

840 Schlup, M., Steck, A., Carter, A., Cosca, M., Epard, J. L., and Hunziker, J., 2011, Exhumation  
841 history of the NW Indian Himalaya revealed by fission track and  $^{40}\text{Ar}/^{39}\text{Ar}$  ages: Journal  
842 of Asian Earth Sciences, v. 40, no. 1, p. 334–350.

843 Searle, M.P., Stephenson, B., Walker, J., and Walker, C., 2007, Restoration of the Western  
844 Himalaya: implications for metamorphic protoliths, thrust and normal faulting, and  
845 channel flow models: Episodes, v. 30, no. 4, p. 242–257.

846 Sorkhabi, R.B., Stump, E., Foland, K.A., and Jain, A.K., 1996, Fission-track and  $^{40}\text{Ar}/^{39}\text{Ar}$   
847 evidence for episodic denudation of the Gangotri granites in the Garhwal Higher  
848 Himalaya, India: Tectonophysics, v. 260, no. 1, p. 187–199.

849 Steck, A., 2003, Geology of the NW Indian Himalaya: *Eclogae Geologicae Helvetiae*, v. 96,  
850 p. 147–196.

851 Stephenson, B.J., Searle, M.P., Waters, D.J., and Rex, D.C., 2001, Structure of the Main  
852 Central Thrust zone and extrusion of the High Himalayan deep crustal wedge, Kishtwar–  
853 Zaskar Himalaya: Journal of the Geological Society, v. 158, no. 4, p. 637–652.

854 Stübner, K., Grujic, D., Parrish, R. R., Roberts, N. M., Kronz, A., Wooden, J., and Ahmad, T.,  
855 2014, Monazite geochronology unravels the timing of crustal thickening in NW  
856 Himalaya: *Lithos*, v. 210–211, p. 111–128.

857 Stüwe, K., and Foster, D., 2001  $^{40}\text{Ar}/^{39}\text{Ar}$ , pressure, temperature and fission track constraints  
858 on the age and nature of metamorphism around the main central thrust in the eastern  
859 Bhutan Himalaya: Journal of Asian Earth Sciences, v. 19, no. 1, p. 85–95.

860 Thakur, V.C., 1998, Structure of the Chamba nappe and position of the Main Central Thrust  
861 in Kashmir Himalaya: Journal of Asian Earth Sciences, v. 16, no. 2, p. 269–282.

862 Thöni, M., 1977, Geology, structural evolution and metamorphic zoning in the Kulu Valley  
863 (Himachal Himalayas, India) with special reference to the reversed metamorphism:



864 Mitteilungen der Gesellschaft der Geologie und Bergbaustudenten in Österreich, v. 24, p.  
865 125–187.

866 Thöni, M., Miller, C., Hager, C., Grasemann, B., and Horschingg, M., 2012, New  
867 geochronological constraints on the thermal and exhumation history of the Lesser and  
868 Higher Himalayan Crystalline Units in the Kullu–Kinnaur area of Himachal Pradesh  
869 (India): *Journal of Asian Earth Sciences*, v. 52, p. 98–116, doi:  
870 10.1016/j.jseaes.2012.02.015.

871 Vance, D., and Mahar, E., 1998, Pressure-temperature paths from PT pseudosections and  
872 zoned garnets: potential, limitations and examples from the Zaskar Himalaya, NW  
873 India: *Contributions to Mineralogy and Petrology*, v. 132, no. 3, p. 225–245.

874 Vannay, J.C., and Hodges, K.V., 1996, Tectonometamorphic evolution of the Himalayan  
875 metamorphic core between the Annapurna and Dhaulagiri, central Nepal: *Journal of*  
876 *Metamorphic Geology*, v. 14, no. 5, p.635–656.

877 Vannay, J.C., Grasemann, B., Rahn, M., Frank, W., Carter, A., Baudraz, V., and Cosca, M.,  
878 2004, Miocene to Holocene exhumation of metamorphic crustal wedges in the NW  
879 Himalaya: Evidence for tectonic extrusion coupled to fluvial erosion: *Tectonics*, v. 23,  
880 no. 1

881 Viete, D.R., Forster, M.A., and Lister, G.S., 2011, The nature and origin of the Barrovian  
882 metamorphism, Scotland:  $^{40}\text{Ar}/^{39}\text{Ar}$  apparent age patterns and the duration of  
883 metamorphism in the biotite zone: *Journal of the Geological Society*, v. 168, no. 1, p.  
884 133–146.

885 Walia, M., Yang, T. F., Liu, T. K., Kumar, R., and Chung, L., 2008, Fission track dates of  
886 Mandi granite and adjacent tectonic units in Kulu–Beas valley, NW Himalaya, India:  
887 *Radiation Measurements*, v. 43, p. 343–347.

888 Walker, J., Martin, M., Bowring, S., Searle, M., Waters, D., and Hodges, K., 1999,  
889 Metamorphism, melting, and extension: Age constraints from the High Himalayan Slab  
890 of southeast Zaskar and northwest Lahul: *The Journal of Geology*, v. 107, no. 4, p. 473–  
891 495.

892 Wang, Y., Li, Q., and Qu, G., 2006,  $^{40}\text{Ar}/^{39}\text{Ar}$  thermochronological constraints on the cooling  
893 and exhumation history of the South Tibetan Detachment System, Nyalam area, southern  
894 Tibet. In: Law, R.D., Searle, M.P., and Godin, L. (Eds), *Channel Flow, Ductile Extrusion*  
895 *and Exhumation in Continental Collision Zones*: Geological Society London, Special  
896 Publications, v. 268, p. 327–354.

897 Warren, C.J., Sherlock, S.C., and Kelley, S.P., 2011, Interpreting high-pressure phengite  
898  $^{40}\text{Ar}/^{39}\text{Ar}$  laserprobe ages: an example from Saih Hatat, NE Oman: *Contributions to*  
899 *Mineralogy and Petrology*, v. 161, no. 6, p. 991–1009.

900 Warren, C.J., Hanke, F., and Kelley, S.P., 2012, When can muscovite  $^{40}\text{Ar}/^{39}\text{Ar}$  dating  
901 constrain the timing of metamorphic exhumation? *Chemical Geology*, v.291, p.79–86.

902 Webb, A.A.G., 2013, Preliminary balanced palinspastic reconstruction of Cenozoic  
903 deformation across the Himachal Himalaya (northwestern India): *Geosphere*, v. 9, no. 3,  
904 p. 572–587.

905 Webb, A.A.G., Yin, A., Harrison, T.M., C  lerier, J., and Burgess, W.P., 2007, The leading  
906 edge of the Greater Himalayan Crystalline complex revealed in the NW Indian Himalaya:  
907 implications for the evolution of the Himalayan orogen: *Geology*, v. 35, no. 10, p. 955–  
908 958.

909 Webb, A.A.G., Yin, A., Harrison, T.M., C  lerier, J., Gehrels, G.E., Manning, C.E., and  
910 Grove, M., 2011, Cenozoic tectonic history of the Himachal Himalaya (northwestern  
911 India) and its constraints on the formation mechanism of the Himalayan orogen:  
912 *Geosphere*, v. 7, no. 4, p. 1013–1061.

913 Wyss, M., 2000, Metamorphic evolution of the northern Himachal Himalaya: Phase equilibria  
 914 constraints and thermobarometry: *Schweizerische Mineralogische und Petrographische*  
 915 *Mitteilungen*, v. 80, no. 3, p. 317–350.

916 Wyss, M., Hermann, J., and Steck, A., 1999, Structural and metamorphic evolution of the  
 917 northern Himachal Himalaya, NW India-(Spiti-eastern Lahul-Parvati valley traverse):  
 918 *Eclogae Geologicae Helvetiae*, v. 92, no. 1, p. 3–44.

919 Zeiger, K., Gordon, S M., Long, S.P., Kylander-Clark, A.R.C., Agustsson, K., and Penfold,  
 920 M., 2015, Timing and conditions of metamorphism and melt crystallization in Greater  
 921 Himalayan rocks, eastern and central Bhutan: insight from U–Pb zircon and monazite  
 922 geochronology and trace-element analyses: *Contributions to Mineralogy and Petrology*,  
 923 v. 169, no. 5, p. 1–19.

924

## 925 **FIGURE CAPTIONS**

926 Figure 1. Overview tectonic map of the NW Himalaya (modified from Stübner et al., 2014).

927 Black rectangle corners outline the extent of Figure 2.

928

929 Figure 2. (A) Geologic map of the study area with own and published thermochronology ages

930 (in  $\text{Ma} \pm 2\sigma$  error). Isograds and metamorphic zones are after Steck (2003) and own

931 observations. In the western part of the study area, published isograds are redrawn to reflect

932 the geometry of the Phojal fold, which folds the metamorphic zones (Epard et al., 1995).

933  $^{40}\text{Ar}/^{39}\text{Ar}$  ages are from this study (Table 2); Rb-Sr ages from Mehta (1977); zircon fission

934 track (ZFT) from Schlup et al. (2011; superscript S) and Walia et al. (2008; superscript W).

935 White outer frame denotes samples from elevation profile near Rohtang pass. (B) Simplified

936 version of Figure 2A showing sample numbers and biotite  $^{40}\text{Ar}/^{39}\text{Ar}$  ages (in  $\text{Ma} \pm 2\sigma$ ). (C)

937 Biotite  $^{40}\text{Ar}/^{39}\text{Ar}$  ages ( $\text{Ma} \pm 2\sigma$ ) projected onto a SSW-NNE profile with 2-times vertical

exaggeration illustrating the large-scale, SW-vergent, recumbent fold in the hanging wall of the Main Central Thrust (MCT). The fold axis of the MCT dips to the NW, therefore the structural position of samples NW and SE of the profile are not accurately reflected by their true elevation above sea level. For samples 827B1, 814G1, 823G2, 823G3, and 819A1, the approximate structural position relative to the MCT and the recumbent fold rather than the sample elevation is shown.

Figure 3. Age spectra and inverse isochrons of  $^{40}\text{Ar}/^{39}\text{Ar}$  analyses; bold labels in lower left indicate sample number and mineral (Ms, muscovite; Bt, biotite), labels in lower right indicate laboratory where analysis was conducted (DGC, Noble Gas Laboratory, Dalhousie, Halifax, Canada; ALF, Argon Lab, Freiberg, Germany). Muscovite  $^{40}\text{Ar}/^{39}\text{Ar}$  data analysed at DGC are from Stübner et al. (2014). Weighted mean ages (WMA) and inverse isochron ages (IIA) are calculated from all data points and/or from subsets of consecutive heating steps that fit a single regression line (grey error boxes and grey error ellipses); for each sample, the same sets of heating steps were used for WMA and IIA calculation. Note that for some samples (e.g., 807D1 Ms, 810B1 Ms, 827B1 Ms) the initial  $^{40}\text{Ar}/^{36}\text{Ar}$  is significantly different from atmospheric composition (295.5), and therefore the IIA, which is independent from atmospheric correction, is the more reliable age compared to the WMA, which is calculated assuming atmospheric initial  $^{40}\text{Ar}/^{36}\text{Ar}$ . MSWD is the mean square of weighted deviates; prob. is the probability of fit (for detailed definitions and discussion, see Ludwig, 2008).

Figure 4. Structural position (top) and lithology of the samples together with their biotite and muscovite  $^{40}\text{Ar}/^{39}\text{Ar}$  ages. Background shading and letters indicate generalized lithology. Small box outlines six ages from an elevation profile near Rohtang pass (marked by outer white box on Figure 2A, B). Biotite  $^{40}\text{Ar}/^{39}\text{Ar}$  ages of samples 823G2 and 823G3 are  $106 \pm 5$

Ma and  $84 \pm 6$  Ma, respectively, and therefore plot outside the diagram. ALF, ArgonLab  
Freiberg; MCT, Main Central Thrust.

Figure 5. Mineralogical composition of biotite separates, determined by Rietveld X-ray  
diffractometry, together with their  $^{40}\text{Ar}/^{39}\text{Ar}$  ages ( $\pm 2\sigma$ ). Separates were obtained by magnetic  
separation and handpicking to remove non-biotite phases; ‘rinsed’ samples were further  
purified by repeated rinsing in deionized  $\text{H}_2\text{O}$  in an ultrasonic bath. All samples dated at ALF  
were rinsed. Note that y-axis starts at 80%, not at zero.

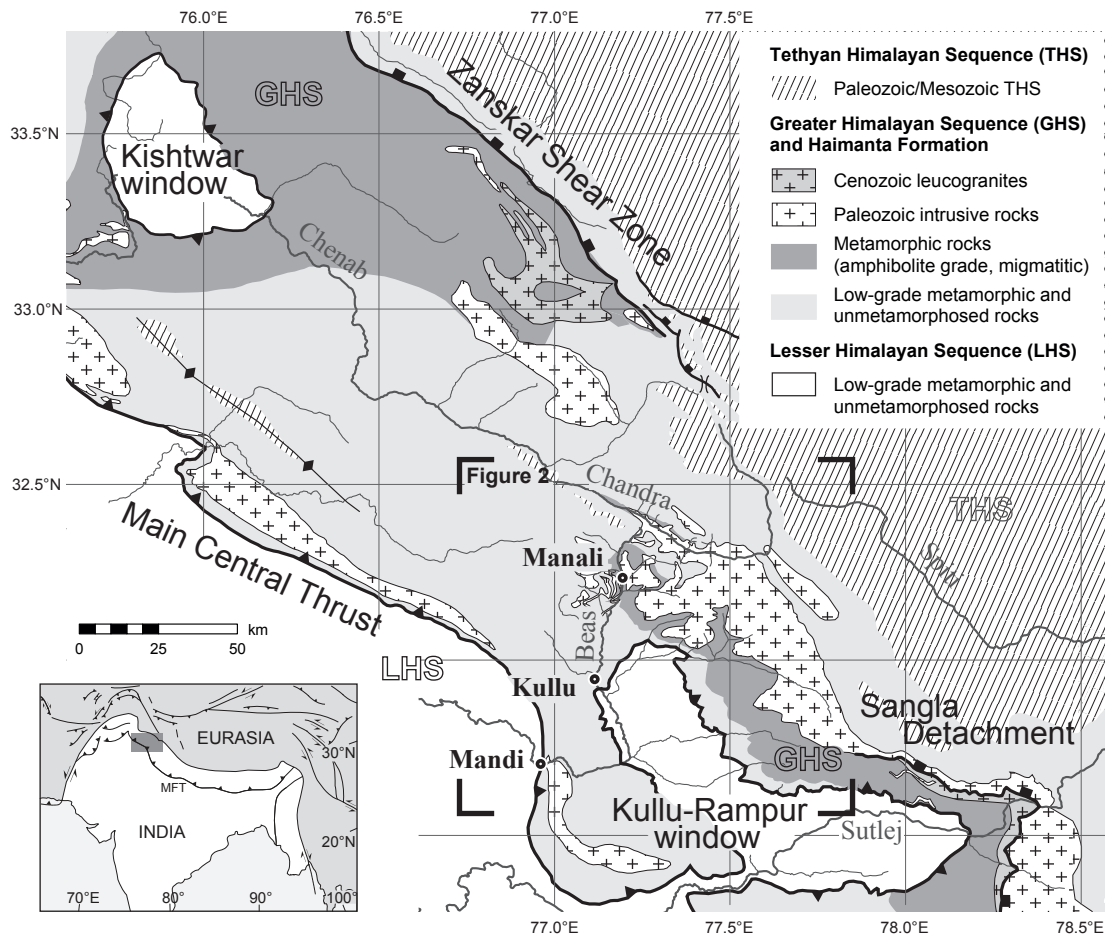
Figure 6. Thermochronologic data (own and published) and regional cooling path for the  
study area (see Figure 2 for geographic locations and references). Yellow and hatched grey  
bands indicate closure temperatures with respective uncertainties. Red arrow indicates the  
approximate cooling path of the crystalline core (red symbols).

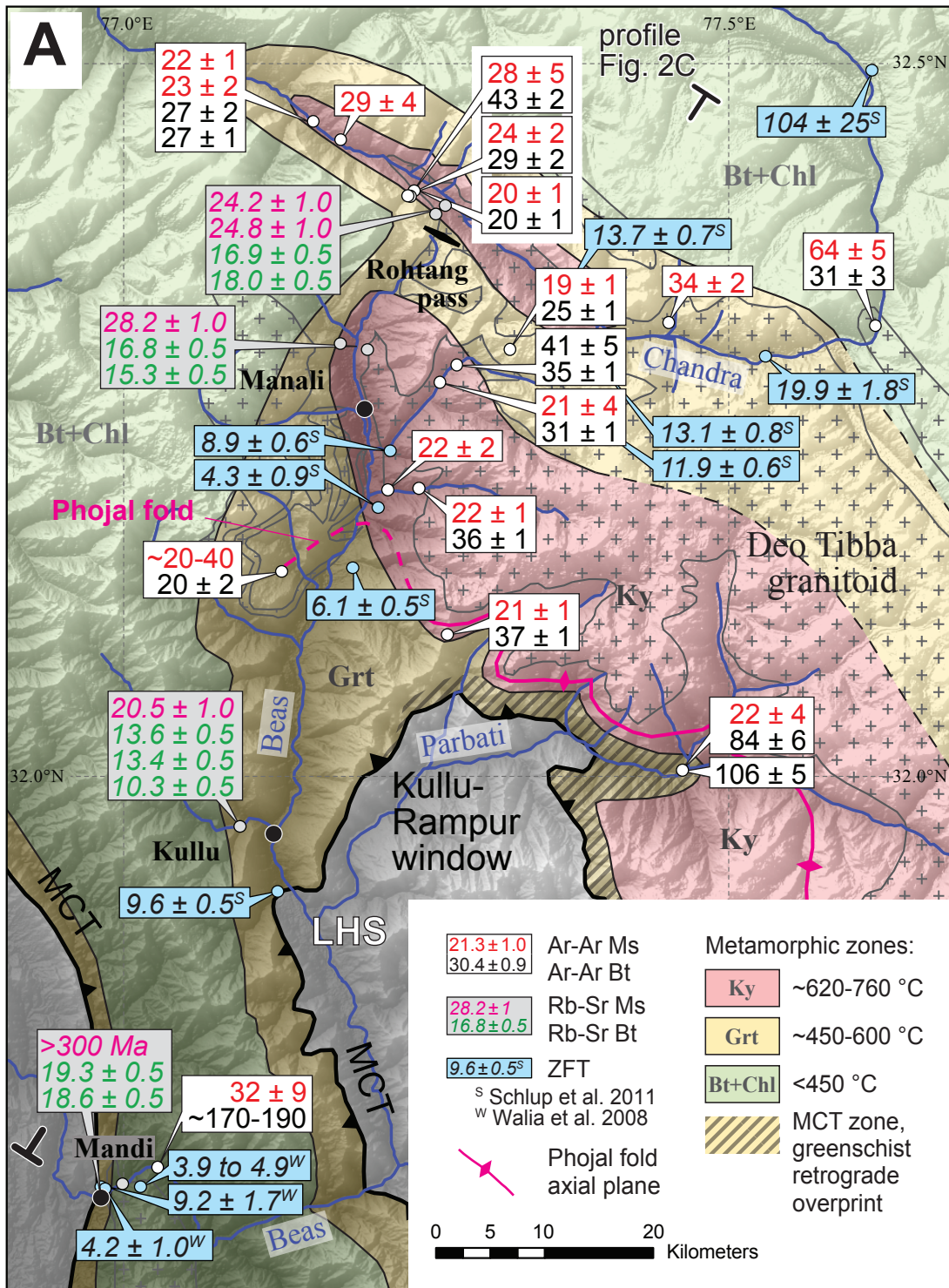
Figure 7. (A) Ti-in-biotite temperatures vs. biotite  $^{40}\text{Ar}/^{39}\text{Ar}$  ages ( $\pm 2\sigma$ ). (B) Initial  $^{40}\text{Ar}/^{36}\text{Ar}$   
ratios vs. inverse isochron ages (both  $\pm 2\sigma$ ) as listed in Table 2.

Figure 8. Schematic diagram illustrating Ar production and movement in and around a biotite  
grain above its closure temperature. The biotite grew or recrystallized dynamically during a  
metamorphic cycle. See text for details.

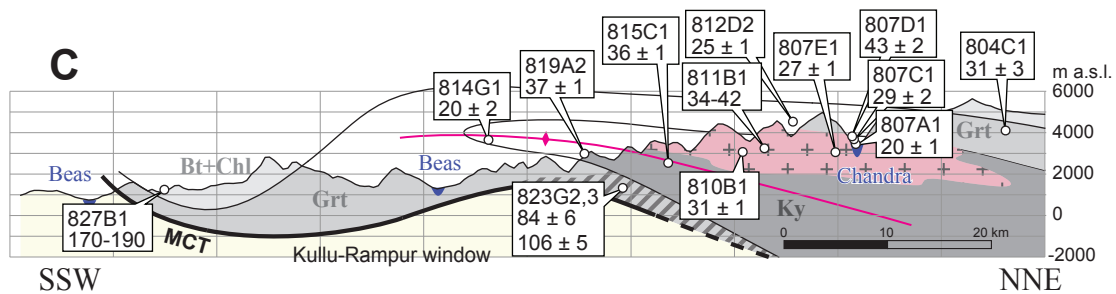
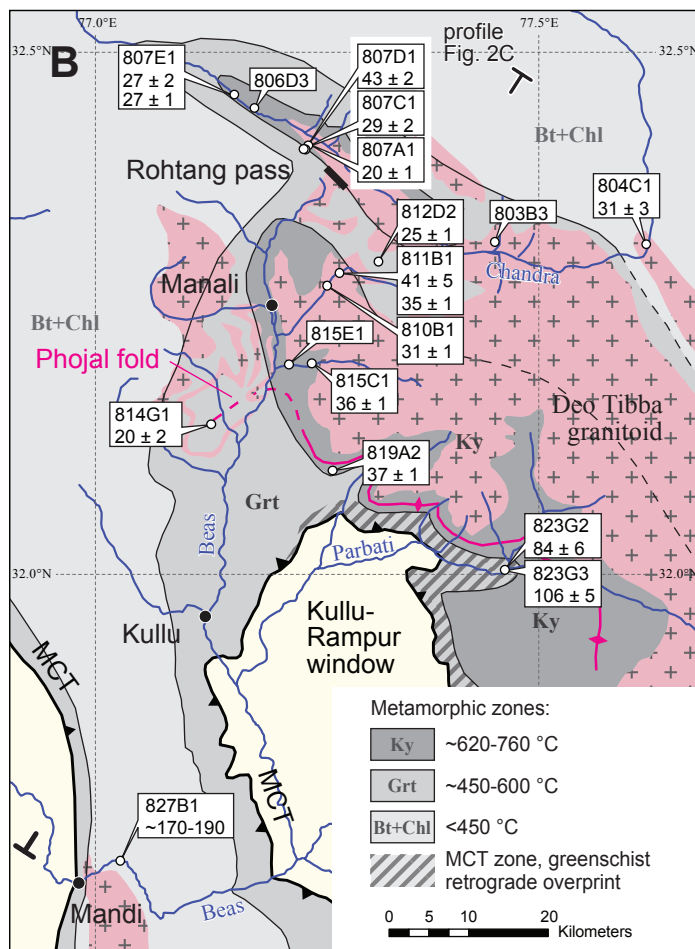
<sup>1</sup>GSA Data Repository item 201Xxxx, including  $^{40}\text{Ar}/^{39}\text{Ar}$  raw data (Tables S1, S2), thin  
section descriptions and photomicrographs (supplemental text and Figure S1), and analytical  
details of  $^{40}\text{Ar}/^{39}\text{Ar}$  analyses and Rietveld X-ray powder-diffractometry (supplemental text) is  
available online at [www.geosociety.org/pubs/ft20XX.htm](http://www.geosociety.org/pubs/ft20XX.htm), or on request from

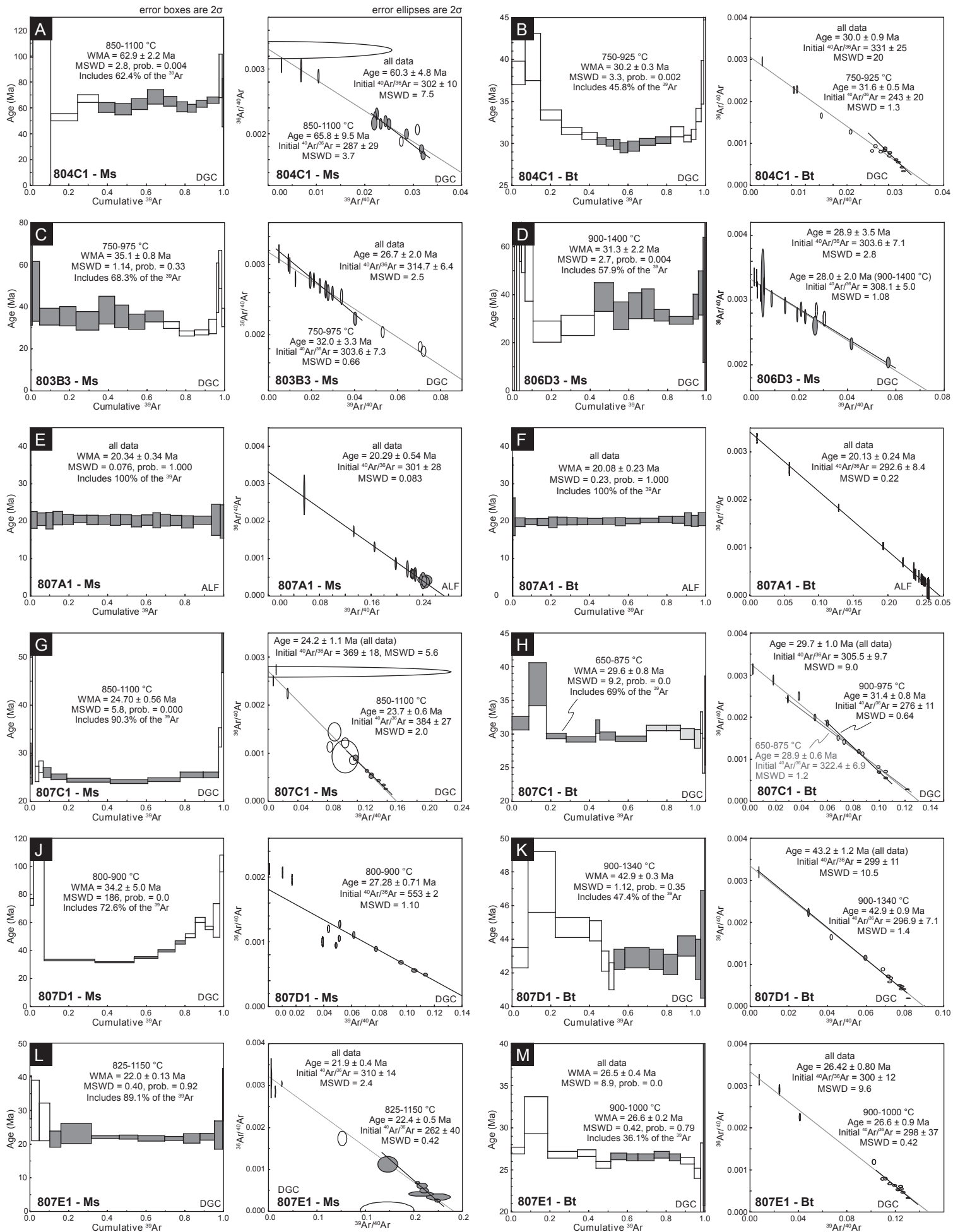
988 editing@geosociety.org or Documents Secretary, GSA, P.O. Box 9140, Boulder, CO 80301,  
989 USA.

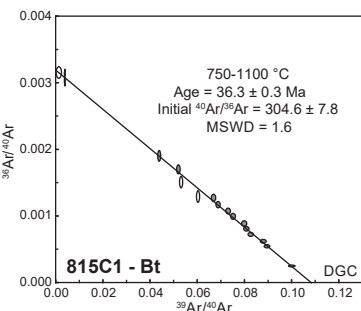
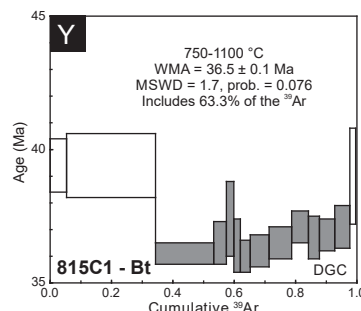
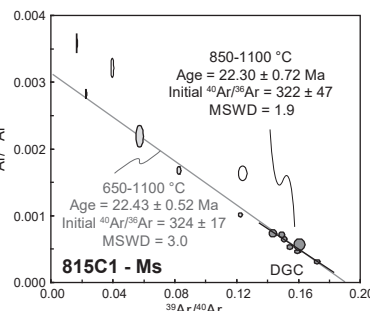
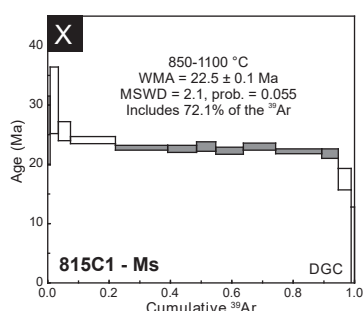
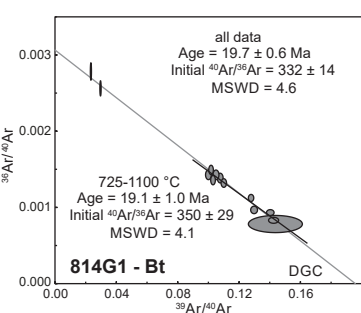
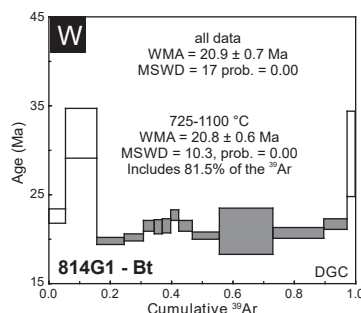
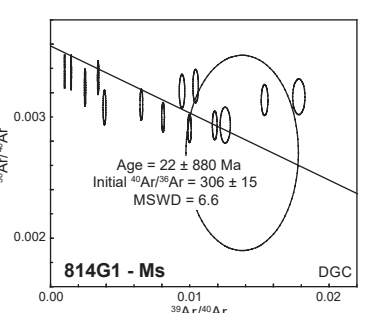
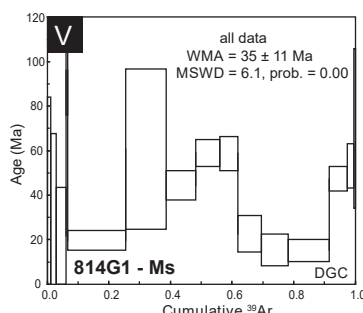
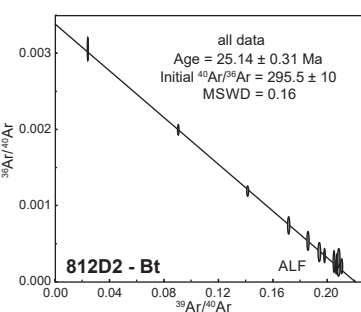
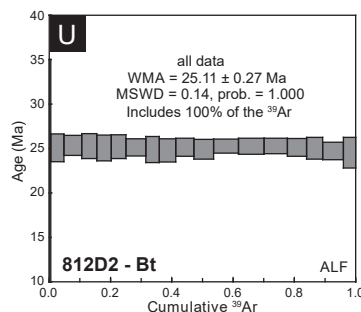
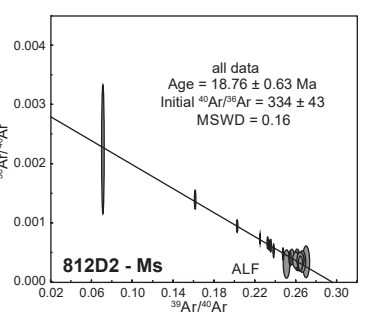
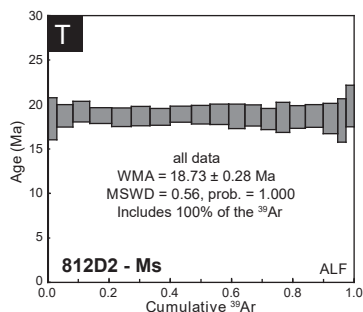
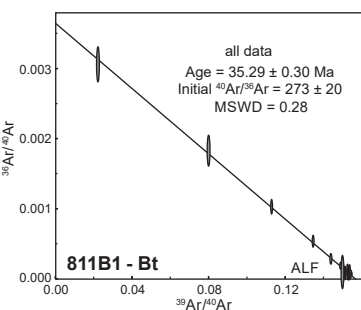
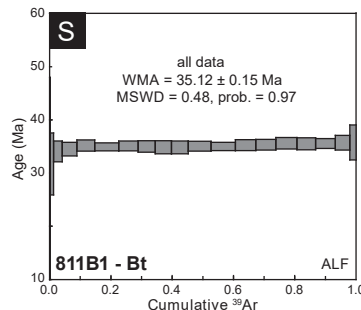
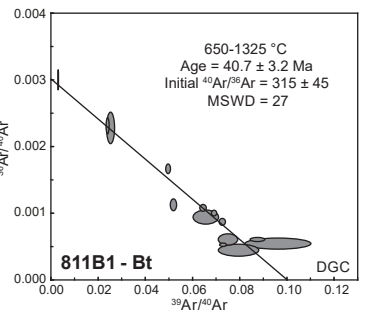
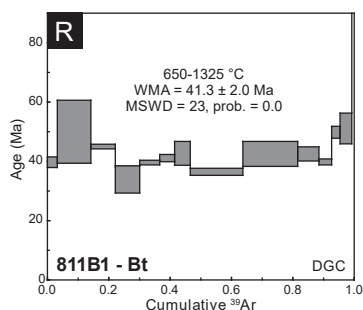
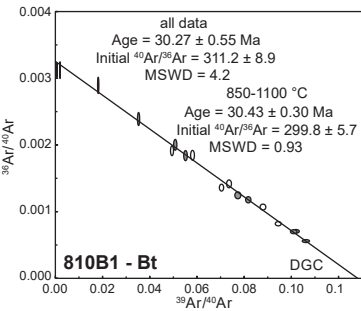
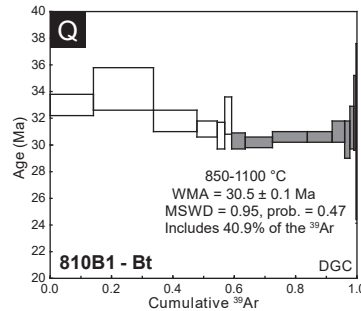
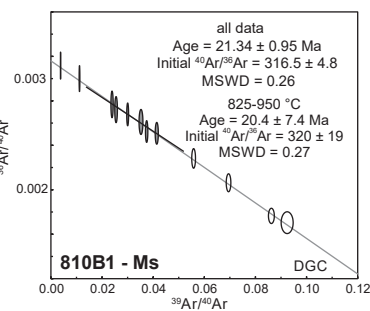
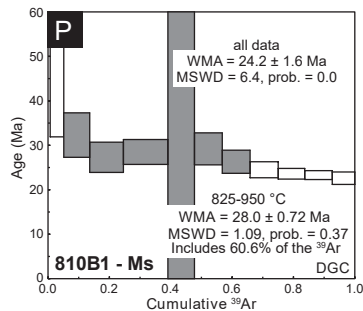
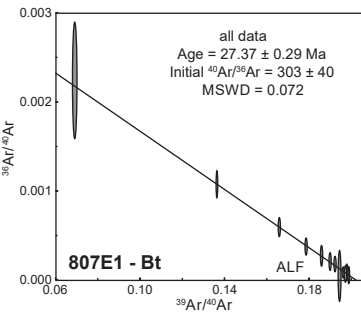
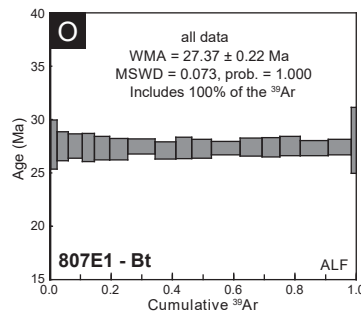
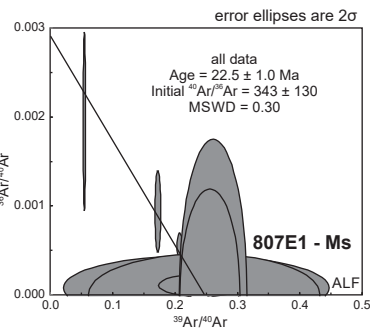
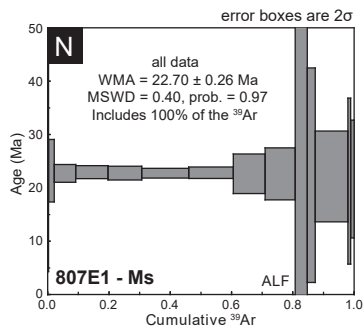


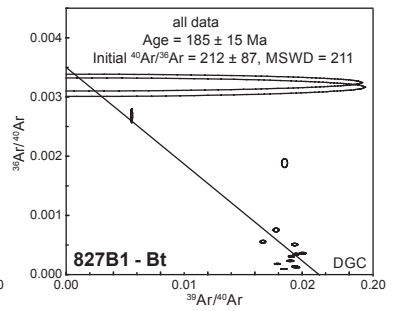
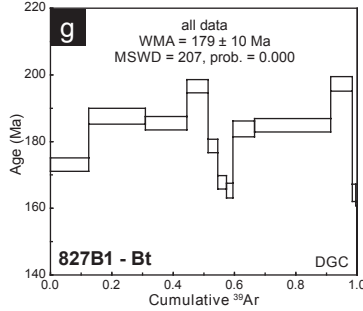
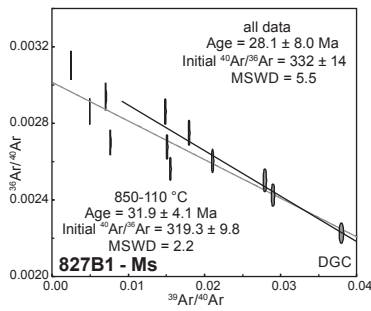
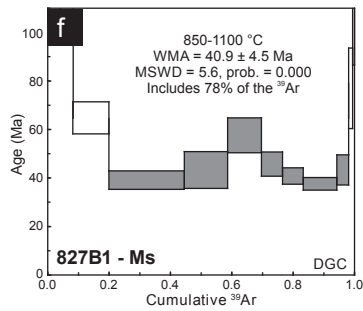
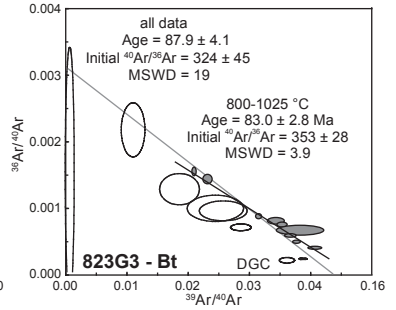
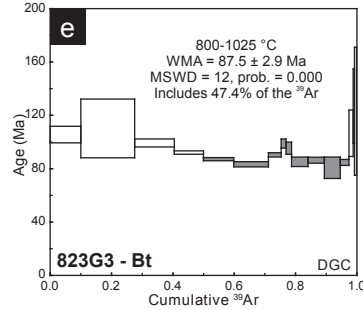
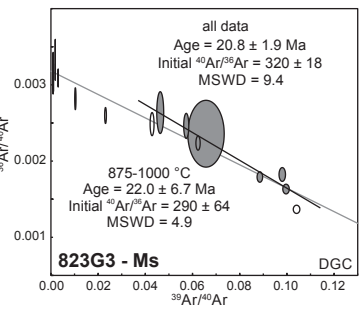
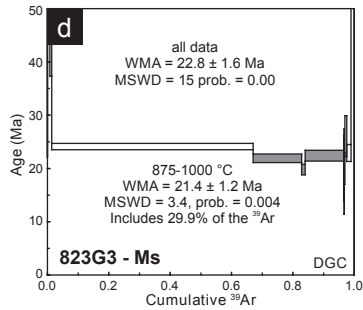
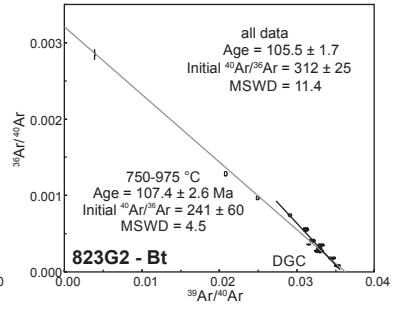
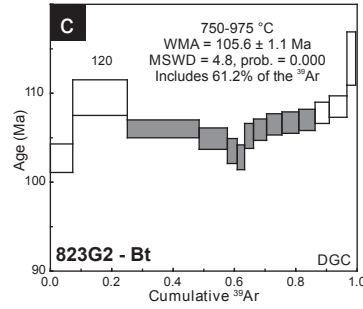
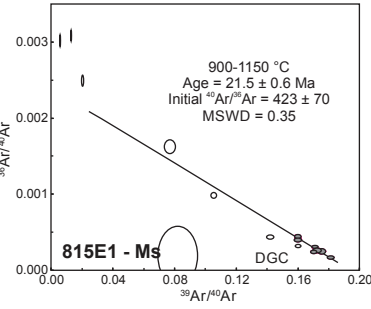
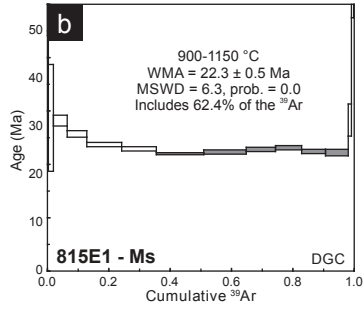
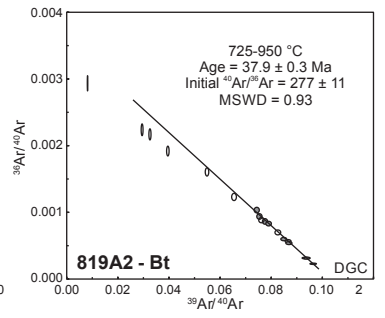
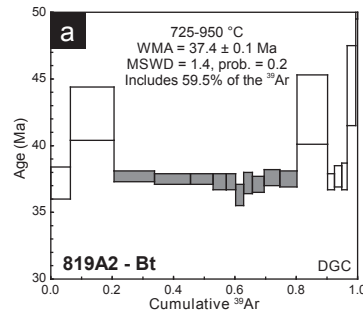
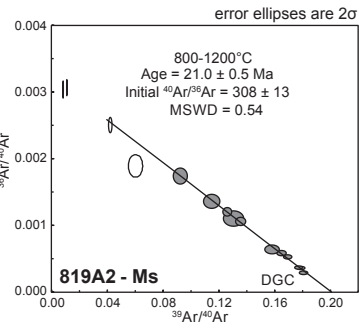
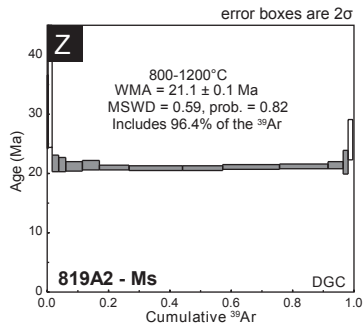


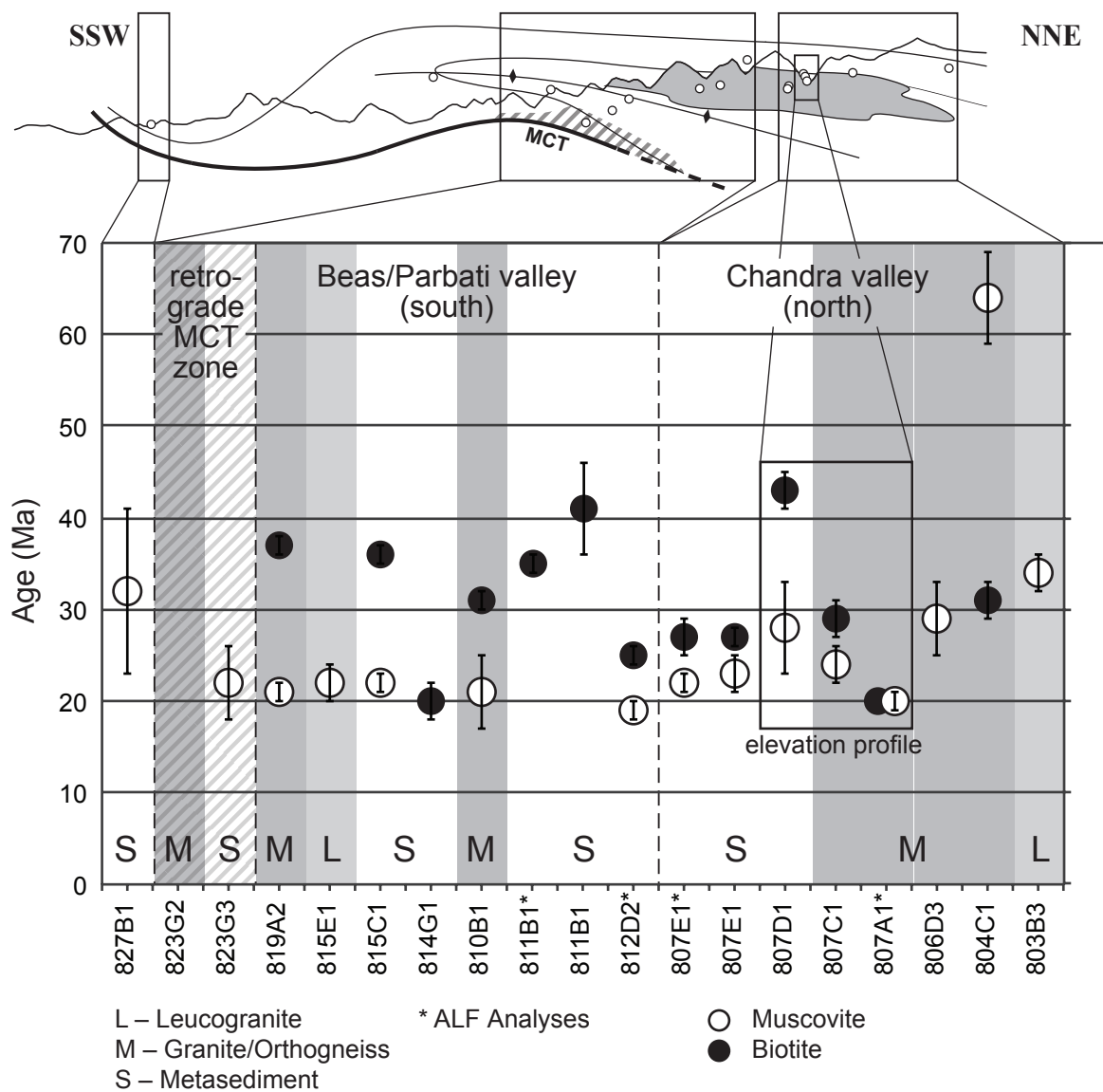


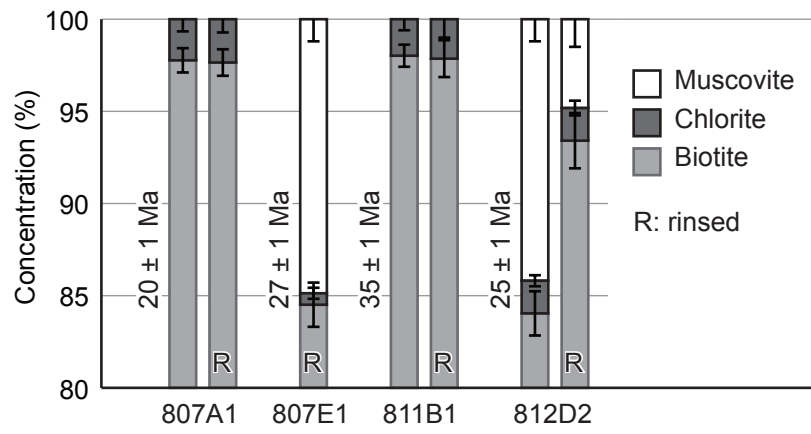


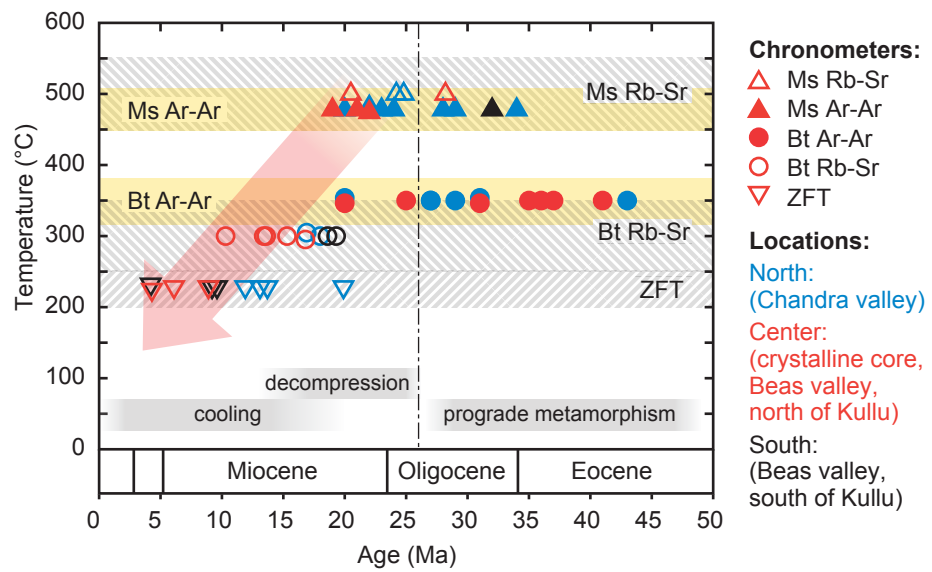


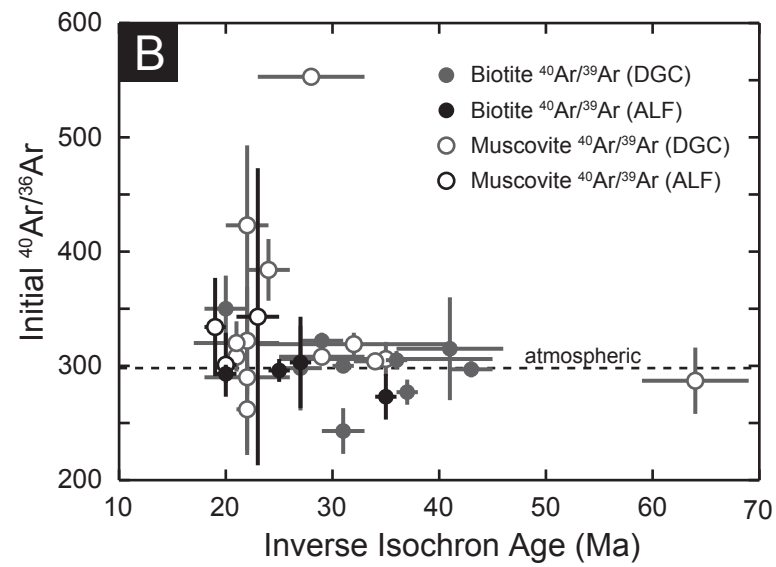
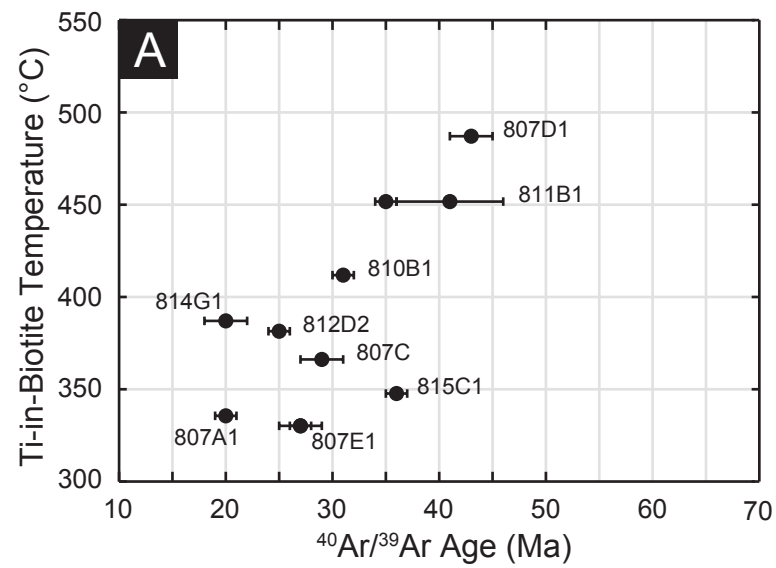














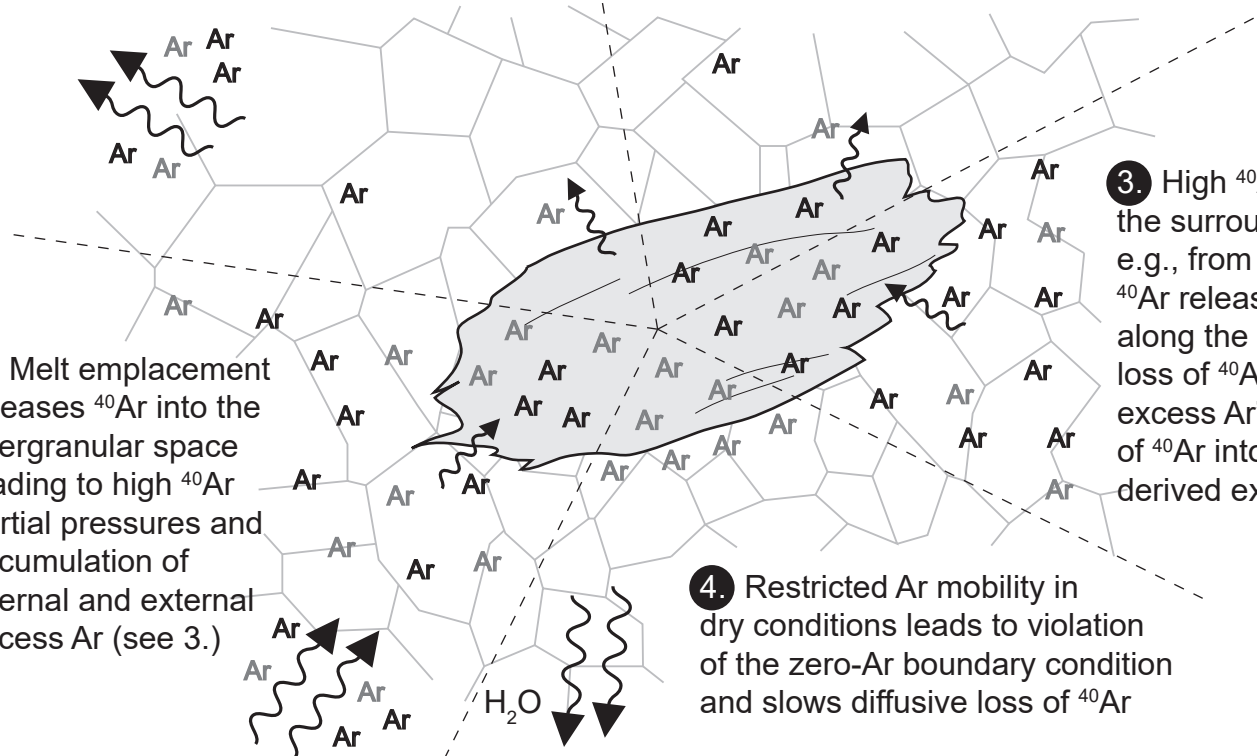
1.  $^{40}\text{Ar}$  released during prograde metamorphism escapes from the system: no accumulation of excess Ar

2. Inherited  $^{40}\text{Ar}$  is trapped, for example, in mineral inclusions or retained in the lattice of the incompletely degassed pre-Cenozoic biotite ("partially reset age")

5. Melt emplacement releases  $^{40}\text{Ar}$  into the intergranular space leading to high  $^{40}\text{Ar}$  partial pressures and accumulation of internal and external excess Ar (see 3.)

3. High  $^{40}\text{Ar}$  partial pressure in the surrounding rock volume, e.g., from prograde metamorphic  $^{40}\text{Ar}$  release or from fluid circulation along the MCT, slows diffusive loss of  $^{40}\text{Ar}$  ("internally derived excess Ar") and facilitates diffusion of  $^{40}\text{Ar}$  into the grain ("externally derived excess Ar")

4. Restricted Ar mobility in dry conditions leads to violation of the zero-Ar boundary condition and slows diffusive loss of  $^{40}\text{Ar}$



Migmatization and melt extraction lead to consumption of hydrous fluids and (temporarily) dry conditions

Ar  $^{40}\text{Ar}$  produced before Cenozoic biotite growth or recrystallization

Ar  $^{40}\text{Ar}$  produced in biotite grain since its Cenozoic (re-)crystallization

Ar may be present in dry or fluid-filled intergranular space and in biotite and other K-bearing and K-free mineral phases according to the respective Ar solubilities

Wiggly arrows indicate diffusion of  $^{40}\text{Ar}$  into and out of the biotite grain (small arrows) and fluid (Ar,  $\text{H}_2\text{O}$ ) exchange between the intergranular space surrounding the biotite and an external reservoir (large arrows)